

Probing the Limit of Heat Transfer in Inorganic Crystals with Deep Learning

Jielan Li^{1†}, Zekun Chen^{1†}, Qian Wang^{1†}, Han Yang^{1*†}, Ziheng Lu^{1*†}, Guanzhi Li¹, Shuizhou Chen¹, Yu Zhu¹, Xixian Liu¹, Junfu Tan¹, Mingfa Tang¹, Yichi Zhou¹, Claudio Zeni¹, Andrew Fowler¹, Daniel Zügner¹, Robert Pinsler¹, Matthew Horton¹, Tian Xie¹, Tie-Yan Liu¹, Haiguang Liu¹, Tao Qin¹, Bing Lv², Davide Donadio^{3*}, Hongxia Hao^{1*}

¹Microsoft Research AI for Science.

²Department of Physics, University of Texas at Dallas, Richardson, TX 75080, USA.

³Department of Chemistry, University of California Davis, Davis, CA 95616, USA.

*Corresponding author(s). E-mail(s): hanyang@microsoft.com;

zihenglu@microsoft.com; ddonadio@ucdavis.edu; hongxiahao@microsoft.com;

†These authors contributed equally to this work.

Abstract

Heat transfer is a fundamental property of matter. Research spanning decades has attempted to discover materials with exceptional thermal conductivity, yet the upper limit remains unknown. Using deep learning accelerated crystal structure prediction and first-principles calculation, we systematically explore the thermal conductivity landscape of inorganic crystals. We brute-force over half a million ordered crystalline structures, encompassing an extensive coverage of local energy minima in binary compounds with up to four atoms per primitive cell. We confirm diamond sets the upper bound of thermal conductivity within our search space, very likely also among all stable crystalline solids at ambient conditions. We identify over 20 novel crystals with high thermal conductivity surpassing silicon at room temperature validated by density functional theory. These include a series of metallic compounds, especially MnV, exhibiting high lattice and electronic thermal conductivity simultaneously, a distinctive feature not observed before. The fast deep learning-driven screening method, as well as the large comprehensive thermal conductivity database, pave the way for the discovery and design of next-generation materials with tailored thermal properties.

Keywords: Lattice Thermal Conductivity, Boltzmann Transport Equation, Machine Learning Potential

1 Introduction

Thermal conductivity (κ) is a fundamental property of matter that characterizes its ability to conduct heat. Understanding the atomic-level mechanisms and pushing the boundaries of thermal conductivity have been central challenges in materials science.[1, 2] Discovering and engineering materials with tailored thermal conductivity, particularly those exhibiting extreme κ , is crucial for a wide range of applications, including thermal management of electronic and photonic devices, heat conductors, thermal insulators, and energy converters.[3–7]

The intriguing question of “what is the upper limit of heat transfer in matter”[1] dates back to Fourier’s time and the quest for an answer has gone hand in hand with the search for extreme thermal conductors (Fig. 1).[2, 8–10] In the 1800s, metals were considered the best thermal conductors, with silver having the highest conductivity ($\sim 430 \text{ W m}^{-1} \text{ K}^{-1}$, Fig. 1). In the 1920s, Peierls discovered that electrons and phonons contribute additively to κ with the former being the dominant heat carriers in metals and the latter in insulators.[11] Diamond was identified as the material with the highest thermal conductivity ($\sim 2000 \text{ W m}^{-1} \text{ K}^{-1}$ at room temperature) with phonon-dominated thermal transport.[12, 13] These mark the early progress in the quest for good thermal conductors, which was majorly driven by phenomenological models and serendipitous experiments. In the last two decades, advancements in the implementation of phonon transport theory have enabled the accurate and systematic computation of thermal conductivity from first principles.[14–17] This approach facilitated the discovery of landmark materials such as boron arsenide (BAs), with a remarkable thermal conductivity initially predicted to be $2240 \text{ W m}^{-1} \text{ K}^{-1}$ at room temperature[18] and later further justified with higher order phonon scattering[19, 20], and confirmed experimentally to be $1000 \pm 90 \text{ W m}^{-1} \text{ K}^{-1}$.[6] This discovery paved the way to the theoretically-driven search for materials with extreme thermal conductivity.[21, 22]

Despite these advances, materials with high κ remain exceptionally rare, and the question of the ultimate limit of heat transfer in matter persists. One hypothesis is that the physical upper bound is set by diamond.[12, 23] However, it is extremely challenging to form a proof (or counter-proof) to such hypothesis. A comprehensive search for high- κ materials across the whole chemical space has been infeasible, bottlenecked by the throughput of characterizations.[24, 25] Experimentally, determining the intrinsic thermal conductivity of inorganic crystalline materials may take several years, as it requires high-quality single-crystal samples and a complex apparatus.[6, 19, 26–29] While first-principles methods offer an alternative by enabling theoretical predictions with desirable accuracy,[14, 16, 17] their computational throughput remains a limiting factor. Recent studies have reached sub-hundred throughput in computing thermal conductivities by solving Boltzmann transport equation (BTE) or running equilibrium molecular dynamics (EMD) from first principles,[30–32]

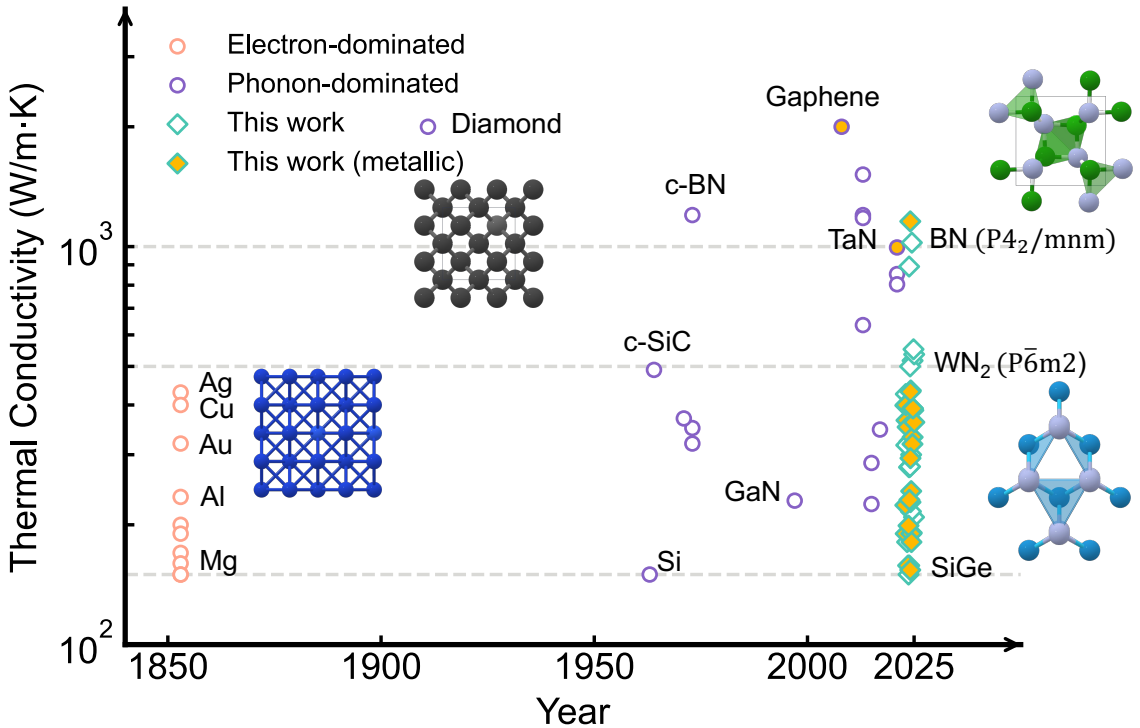


Fig. 1: Historical overview of high thermal conductivity materials alongside newly identified candidates from this work. Thermal conductivity values from the literature are listed in Table S5, while newly identified data are presented in Table 1, which are obtained from Boltzmann transport equation calculations based on DFT. The scattering effects considered in these calculations have been listed in Table 1. Materials represented by yellow-filled symbols indicate metallic compounds.

but a systematic exploration of the wide space of different crystalline prototypes and chemical systems has been infeasible.

In this Article, we present an extensive characterization of the thermal conductivity for inorganic materials using deep learning accelerated atomistic simulations with near first-principles accuracy. In particular, we search for materials with high thermal conductivity and explore the limit of heat transfer by brute-forcing both the chemical and structural space of inorganic crystals via large-scale crystal structure prediction and high-throughput thermal conductivity calculations. A total of 642,603 structures were characterized for their vibrational properties, among which 236,574 dynamically stable crystals were studied for their thermal conductivity. The extensive search leads to the following main findings: (1) We carry out the most exhaustive search of elemental and binary ordered crystals to date, and confirm that diamond sets the upper limit of thermal conductivity of the searched structures. (2) Despite the extreme sparsity of high thermal conductors in materials space, we found over 20 novel structures (Fig. 1) with thermal conductivity exceeding that of silicon at room temperature ($145 \text{ W m}^{-1} \text{ K}^{-1}$). (3) New binary metallic compounds with efficient phononic transport were discovered, having lattice thermal conductivity 10-fold higher than the lattice counterpart of conventional

metals. In particular, the intermetallic compound MnV stands out for lattice and electronic thermal conductivity both high and of comparable magnitude, resulting in a total thermal conductivity of $243 \text{ W m}^{-1} \text{ K}^{-1}$, akin to aluminum.[33] This is a newly discovered distinctive thermal transport behavior. This study redefines current knowledge of thermal conductivity landscape for crystalline materials over an expansive space by providing a detailed characterization of more than 236,000 materials with near first-principles accuracy incorporating three-phonon scattering processes. The large database serves as a rich foundation for tailored design of materials to meet specific thermal management requirements for the community.

2 Search space for high thermal conductivity materials

We constructed a workflow to generate an extensive database of the lattice thermal transport properties of inorganic crystals, see Fig. 2a and subsection S1.1. Following Slack's seminal work,[38] we first focus on simple crystalline structures that are most likely to exhibit high thermal conductivity to challenge the diamond limit. We systematically traverse 3,240 binary chemical systems and carry out random structure searches (RSS)[39, 40] for local energy minima with up to four atoms per unit cell within these systems (Fig. S1). Given the exhaustive nature of this approach,[40] this pool effectively spans both the compositional and structural space under these constraints. A loose stability threshold of 0.2 eV/atom above the convex hull is set to avoid overlooking structures that may be kinetically stable under ambient conditions. In total, this provides a pool of 113,381 candidate structures.

In addition to this pool, we further incorporate 529,222 more complex structures with more atoms in the unit cell, more chemical species, or higher energy above the convex hull (see Fig. S1 for details). While increased structural complexity generally leads to stronger phonon scattering and reduces the probability of achieving extreme thermal conductivity, they broaden the search space, thereby increasing the likelihood of discovering novel high- κ candidates. Adding these complex structures leads to a pool that contains 642,603 structures.

Using a deep learning atomistic model MatterSim,[41] we assess the dynamical stability of each structure within this extensive dataset under harmonic approximation. This leads to 236,574 structures that are dynamically stable for which we compute the thermal conductivity using the Boltzmann transport equation in the relaxation time approximation with three-phonon scattering. As shown in Fig. 2b, the current candidate pool is not only several orders of magnitude larger in sheer number compared with previous studies, but also warrants a much less biased sampling of both the chemical and structural space.

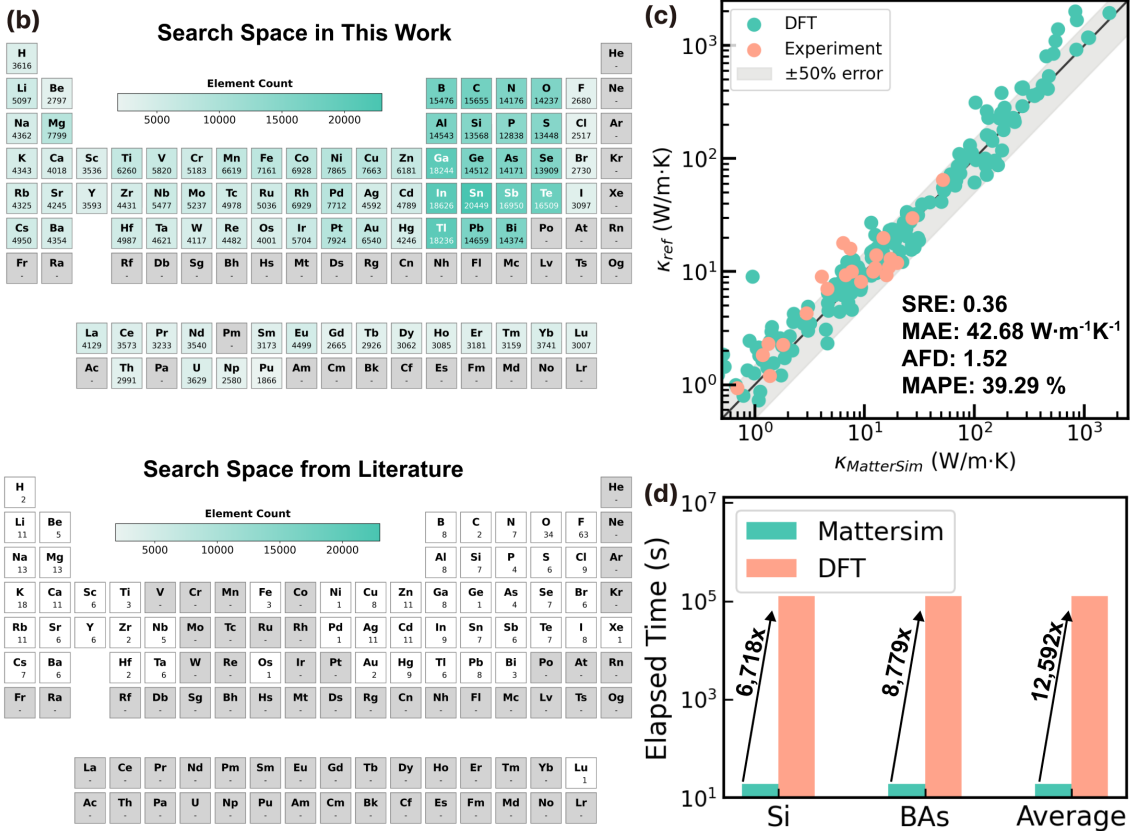


Fig. 2: Deep learning accelerated thermal conductivity screening. (a) Computational workflow. The initial structure database is sourced from deep learning accelerated random structure search and existing databases. Dynamically stable structures were computed for their thermal conductivity, leading to the final MatterK database; (b) Comparison of current search space between this work and previous studies[25, 32, 34–36]. (c) Parity plot comparing computed thermal conductivity and reference values. Average Factor Difference (AFD), Symmetric Relative Error (SRE)[37], Mean Absolute Error (MAE), and Mean Absolute Percentage Error (MAPE) are computed as statistical metrics for model accuracy. (d) Elapsed time computing third-order force constant by MatterSim and DFT on Si, BAs, and an average over 93 materials. One Nvidia A100-80G GPU was used for deep learning accelerated computation while two Nvidia A100-40G GPU were used for DFT computation.

3 Deep learning accelerated first-principles characterization

Reliable prediction of lattice thermal conductivity from atomistic simulations requires an accurate and transferable method to describe both harmonic phonon properties and higher-order anharmonic interactions.[2, 14] Density functional theory (DFT)[42, 43] or empirical potentials has been widely used for such tasks.[14, 24, 44] However, the large size of the current structure pool requires computational efficiency and high accuracy. Here, we employ MatterSim, a deep learning foundation model for

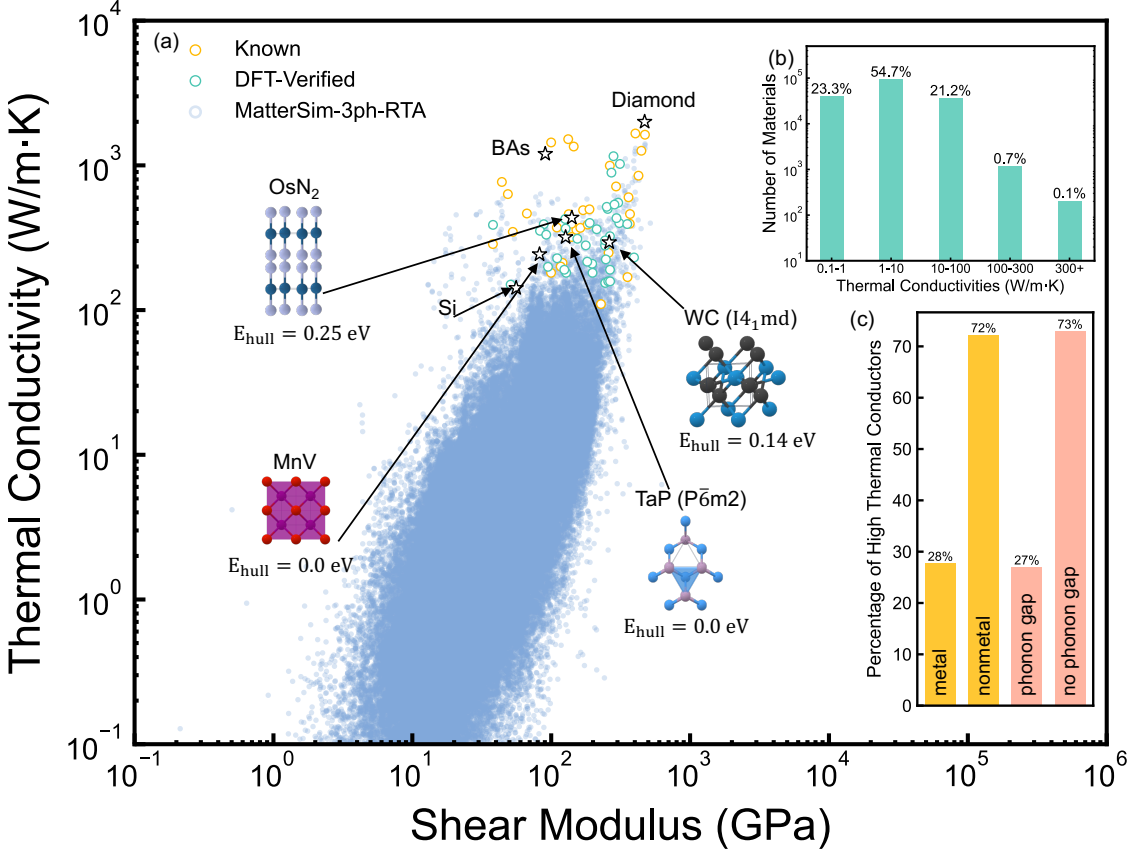


Fig. 3: Thermal conductivity distributions in MatterK database. (a) Lattice thermal conductivities under the three-phonon scattering process as a function of shear modulus, predicted by MatterSim for bulk crystals in the MatterK dataset (blue). Known high thermal conductors from the literature are highlighted in orange, while DFT-verified new high thermal conductor candidates are shown in purple. (b) The distribution of the lattice thermal conductivity for these structures in different ranges. (c) The classification of high thermal conductors in MatterK dataset based on whether they are metallic or non-metallic and whether their phonon dispersion exhibit a phonon gap.

atomic systems across the periodic table trained over a broad range of temperatures and pressures.[41] The model achieves state-of-the-art predictions of phonon properties of inorganic crystals[41, 45] and mitigates the phonon softening issues,[46] with high computational efficiency. During the development of this study, we notice that a few recent researches[37, 47] that also prove the feasibility of applying universal machine learning potentials to predict lattice thermal conductivity of inorganic crystals.

We first benchmark the model on thermal conductivity using Boltzmann transport equation with three-phonon scattering (3ph-BTE) against DFT calculations and experiments (Fig. 2c). The results demonstrate MatterSim’s predictive accuracy across materials with thermal conductivities spanning from 1 to $2000 \text{ W m}^{-1} \text{ K}^{-1}$. This benchmark dataset, constructed through random sampling and integration of existing data, encompasses a diverse set of materials, including oxides, nitrides, and phosphides. As shown in Fig. 2c, validation against both first-principles calculations and experimental measurements reveals a strong linear correlation between MatterSim’s deep learning accelerated predictions and reference values. The model achieves errors of 0.36 (symmetric relative error, SRE),

$42.68 \text{ W m}^{-1} \text{ K}^{-1}$ (mean absolute error, MAE), 1.52 (average factor difference, AFD), and 39.29 % (mean absolute percentage error, MAPE), exhibiting high predictive accuracy,[37] especially for materials with high thermal conductivities, as detailed in [Table S2](#). On the speed side, 3ph-BTE calculations using MatterSim (MatterSim-BTE) are at least 1,000 times faster than conventional first-principles methods. As shown in the lower panel of [Fig. 2d](#), an average acceleration factor of up to 10^4 times can be achieved, reducing the computational time from weeks to minutes.

Leveraging the AI-accelerated MatterSim-BTE calculator, we carried out third-order force constants and 3ph-BTE calculations for the 236,574 dynamically stable structures to determine their lattice thermal conductivity, and created MatterK, a comprehensive database of lattice thermal conductivities at the level of BTE with three-phonon scattering under the single mode relaxation time approximation (RTA). The distribution of computed thermal conductivity is plotted in [Fig. 3a](#) against the shear modulus of the materials which exhibits the strongest correlation coefficient in our Pearson's analysis ([Fig. S6](#)). Additional distributions of κ with respect to other parameters such as symmetry are provided in [Fig. S7](#) and [Fig. S8](#).

4 The upper limit

For decades, researchers have pursued materials with exceptionally high thermal conductivity but have been unable to surpass the record set by diamond. This leads to one key hypothesis: diamond represents the fundamental physical limit for heat transfer in matter under ambient conditions. Forming a proof of this claim has been challenging — it is difficult to derive an analytical bound due to the intricacies of phonon transport and the multitude of factors governing heat conduction. We testify this hypothesis by an extensive search of possible simple crystalline structures that may stably exist as described in [Section 2](#). We carried out 3ph-BTE calculations on all these potential structures. Such computations provide an upper boundary to κ as they do not account for higher-order phonon scattering and other extrinsic processes. It is worthwhile to note that, a very small fraction of structures stood out from the search with κ exceeding $500 \text{ W m}^{-1} \text{ K}^{-1}$, like $\bar{\text{P6m2-WC}}$ [21]. Considering the deep learning error range, they could potentially break the diamond bound. A further DFT verification confirms none of these structures has thermal conductivity exceeding diamond, as shown in [Fig. 3a](#). With these, we confirm diamond to set the limit under ambient condition within the searched structures, i.e., binary compounds with up to four atoms per unit cell.

Beyond this space, it is difficult to further carry out extensive search for local energy minima on the potential energy surface, considering the increasing number of degrees of freedom. However, our analysis reveals a general observation that the thermal conductivity of a ternary compound tend not to exceed the highest value observed among the corresponding binary constituents (see [Fig. S4](#) and [Fig. S5](#)). For example, while BC_2N and MoWC_2 exhibit exceptionally high κ_{ph} values,

they remain below the maximum thermal conductivity found in their respective binary counterparts. Notably, this trend holds consistently for ternary compound with thermal conductivity exceeding $300 \text{ W m}^{-1} \text{ K}^{-1}$. Furthermore, when additional scattering mechanisms and electron contributions are considered, some candidates with initially high thermal conductivity, such as HfP, MoWC₂ and more illustrated in [Table S6](#), undergo significant reductions in their predicted thermal conductivity values. As a result, the pool of viable ultrahigh thermal conductivity materials narrows down considerably, leaving only C, BN, and BC₂N (in different phases), as confirmed by first-principles computations. Therefore, given the extensive exploration of binary systems and the constraints imposed by phonon transport physics, diamond is very likely to also set the physical limit of ambient thermal conductivity throughout the entire materials space.

5 High thermal conductivity materials

While it is unlikely that any bulk crystal will break the diamond limit, we identified a large pool of dynamically stable structures with potential high thermal conductivity greater than silicon. From the distribution in [Fig. 3b](#), we observe that the vast majority of crystalline materials exhibit lattice thermal conductivities in the range of $1 \text{ W m}^{-1} \text{ K}^{-1}$ to $10 \text{ W m}^{-1} \text{ K}^{-1}$, with fewer than 1% exceeding $100 \text{ W m}^{-1} \text{ K}^{-1}$ [Fig. 3b](#). This rarity underscores why, despite centuries of search, compounds with exceptionally high thermal conductivity have remained elusive. Nevertheless, under three-phonon approximation, we identified 968 structures with lattice thermal conductivities exceeding that of silicon, representing the largest dataset of high thermal conductivity crystalline materials compiled to date. In particular, 112 of them show a thermal conductivity over $500 \text{ W m}^{-1} \text{ K}^{-1}$. Many of these structures belong to compositional and structural ranges previously unknown. For example, a set of high thermal conductivity candidates was identified with previously unreported chemical compositions with distinct structure features, including OsN₂, MoWC₂, MnV, ReB, I₂3-CH[48], Be₂CoNi, and WN₂. We also identified a unique family of materials, exemplified by OsN₂, that share a one-dimensional (1D)-chain-like structure with P6 symmetry. These materials, which include OsC₂, ReN₂, RuN, NbF, CoN, TiF, TcF, and IrN, exhibit ultrahigh thermal conductivity along the z-direction. Unfortunately, they are typically characterized by high formation energies, suggesting substantial thermodynamic instability.

Among the large pool of 968 deep learning-prescreened high- κ structures, we have validated ~ 20 most promising newly identified thermal conductors through first-principles three phonon-BTE calculations - a number comparable to the total count of historically known high thermal conductivity materials ([Table S5](#)). Notably, a substantial fraction of these materials exhibits phonon gaps, similar to BAs, while a significant proportion are metallic ([Fig. 3c](#)). These findings highlight the necessity of incorporating higher-order phonon interactions and electron-phonon coupling in thermal transport

models. Given the high computational costs to assess four-phonon and electron-phonon scattering by first principles, we performed full calculation for only a subset of these materials ([Table 1](#)), acknowledging that κ of some currently identified high thermal conductivity candidates may be overestimated once all scattering mechanisms are considered.

Table 1: Potential high- κ candidates verified by DFT. The structures are sourced from the Materials Project database (labeled with MP IDs) and an in-house random structure search database (labeled with RSS). The energy above the convex hull, E_{hull} , is reported in eV/atom, where higher values indicate greater thermodynamic instability for synthesis. The scattering process column specifies the different scattering processes considered in the DFT-BTE calculations. Determination of whether a structure is metallic or semiconductive is based on DFT calculations with PBE functional.

Category	Systems	ID	Space Group	E_{hull}	Thermal conductivity κ (W m ⁻¹ K ⁻¹)			
					xx	yy	zz	scattering process
Semiconductors and Insulators	B ₆ O	mp-1346	R̄3m	0.00	279	279	206	A
	B ₆ P	mp-28395	R̄3m	0.00	209	209	189	A
	SiGe	mp-1219182	F̄43m	0.02	150	150	150	A
	WN ₂	mp-999549	P̄6m2	0.09	436	436	517	A
	WN ₂	mp-1077232	P̄6 ₃ /mmc	0.09	300	300	303	A
	BP	RSS	R̄3m	0.11	426	426	342	A
	BP	RSS	P̄6m2	0.14	388	388	244	A
	BN	mp-13151	P̄4 ₂ /mnm	0.18	451	451	1023	A
	PtN ₂	mp-1095618	Pā3	0.21	216	216	216	A
	BN	mp-644751	Pnma	0.27	266	500	356	A
	BN	mp-1077506	Imm2	0.30	184	304	324	A
	CH [†]	mp-1079612	I ₂ 1 ₃	0.32	536	536	536	A
	CN ₂	mp-1009818	Ī4m2	0.73	399	399	216	A
Metallic	AlGaN ₂	mp-1228894	P3m1	0.01	181	181	144	A
	AlSiCN	mp-1227998	P3m1	0.04	317	317	275	A
	BeSiN ₂	mp-1227309	P3m1	0.17	280	280	102	A
	BC ₂ N	mp-1078541	C ₂ /m	0.64	400	891	623	A
	BC ₂ N	mp-1008523	P4m2	1.00	552	552	487	A
	TaP*	mp-1187244	P̄6m2	0.00	230	230	366	D
	MnV*	mp-316	Pm3m	0.00	243	243	243	D
	NbB	mp-2580	Cmcm	0.00	400	319	312	A
	HfS	mp-1206743	P̄6m2	0.00	247	247	352	A
	VCr	RSS	Pm̄3m	0.00	332	332	332	A
	TaP	mp-1067587	I ₄ 1md	0.00	319	319	136	A
	VB	RSS	Fm̄3m	0.00	228	228	228	A
	ReB	RSS	P̄6m2	0.00	90	90	158	C
	TaRe	RSS	Pm̄3m	0.00	191	191	191	A
	VN	mp-1018027	P̄6m2	0.00	157	190	157	A
	TaW	RSS	Pm̄3m	0.00	190	190	190	A
	WB ₂	RSS	R̄3m	0.00	118	118	158	A
	ReN	RSS	R̄3m	0.01	181	181	146	A
	CrC	mp-1018050	P̄6m2	0.08	174	174	224	A
	WC	RSS	I ₄ 1md	0.14	294	294	198	C
	OsN ₂	mp-973935	P6/mmm	0.25	112	112	435	D
	BC ₅	mp-1077125	Ī4m2	0.25	393	393	242	A
	BC ₇	mp-1079046	Pmm2	0.25	231	206	163	A
	ReC	mp-1009735	P̄6m2	0.27	225	225	362	A
	TiN	mp-998908	F43m	0.30	199	199	199	A
	C	mp-1008374	Cmmm	0.44	237	620	1157	A
	MnCrV ₂	mp-864953	Fm̄3m	0.00	392	392	392	A
	MoWC ₂	mp-1221393	Pmm2	0.00	154	117	91	C
	B ₂ CN	mp-1079333	Pmma	0.24	373	432	215	A

* LDA functional is adopted in DFT calculations.

† K_4 phase of the carbon-hydrogen compound identified in Ref. [48](#).

A: 3-phonon scattering.

B: 3-phonon plus 4-phonon plus isotope scattering.

C: 3-phonon plus phonon-electron plus isotope scattering with electron thermal conductivity.

D: 3-phonon plus 4-phonon plus phonon-electron plus isotope scattering with electron thermal conductivity.

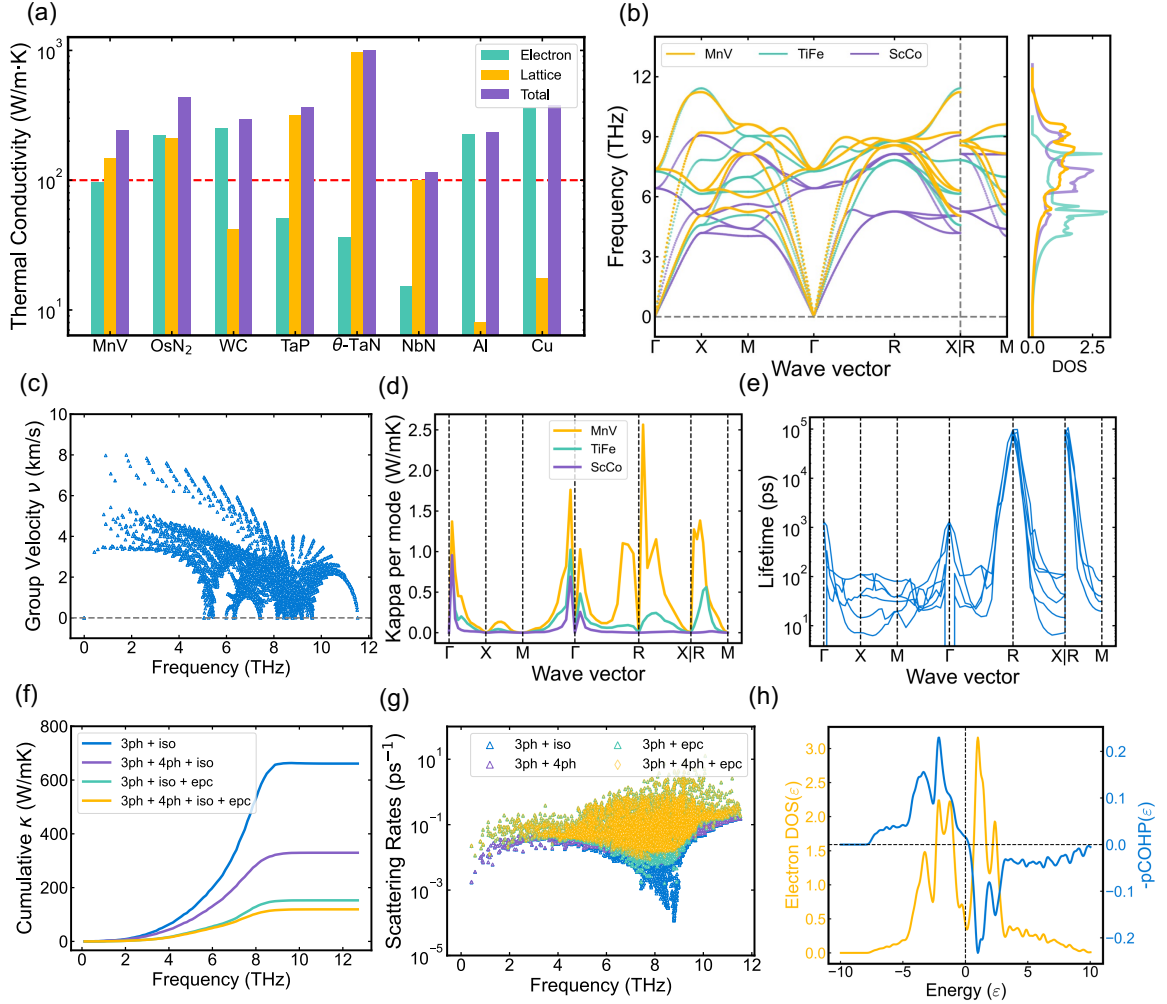


Fig. 4: (a) The electron part, lattice part and total of thermal conductivities for metallic systems with high thermal conductivity. (b) Phonon dispersion and density of states for MnV, TiFe and ScCo. (c) Group velocity for MnV. (d) κ per mode along high symmetry points path for MnV, TiFe and ScCo. (e) Lifetime of different phonon bands along high symmetry points path for MnV. (f) Cumulative thermal conductivities for MnV considering different scattering mechanism (“3ph”, “4ph”, “iso” and “epc” represent three-phonon process, four-phonon process, isotopes effect and electron-phonon coupling effect, respectively). (g) Scattering rates for MnV. (h) Electronic density of states (DOS) and projected crystal orbital Hamilton population (pCOHP) for MnV.

6 Metallic compounds with high lattice thermal conductivity

The thermal conductivity of crystalline materials sums up the contributions of two energy carriers: electrons and quantized lattice vibrations, i.e. phonons. Conventional metals such as copper ($400 \text{ W m}^{-1} \text{ K}^{-1}$), aluminum ($237 \text{ W m}^{-1} \text{ K}^{-1}$), and iron ($80 \text{ W m}^{-1} \text{ K}^{-1}$) exhibit high electronic thermal conductivity (κ_{el}) but very low phononic conductivity (κ_{ph}). In contrast, a small subset of metallic and semi-metallic compounds have been recently found to have anomalously high κ_{ph} but relatively low κ_{el} , including θ -Ta_N,^[22] NbN,^[49] P $\bar{6}$ m2-WC,^[21] I4₁md-WC (this work), and P $\bar{6}$ m2-TaP (this work). However, materials with significant contributions from both electron and phonon transport remain missing, to the best of our knowledge.

We identify two metallic compounds MnV and OsN₂ that simultaneously exhibit both exceptionally high κ_{el} and κ_{ph} (Fig. 4a). Notably, MnV has $\kappa_{\text{el}} \sim 100 \text{ W m}^{-1} \text{ K}^{-1}$, and a lattice thermal conductivity of $120 \text{ W m}^{-1} \text{ K}^{-1}$ computed from first principles, a relatively high value for a metallic compound consisting of two heavy atoms. The unique characteristics of this material arise from a combination of several factors, as explained below. MnV crystallizes in a *bcc* structure, that features 3-fold degeneracy of both acoustic and optical phonons at the high-symmetry *R* point, with only a small frequency difference between the two branches (Fig. 4b). Such patterns in phonon dispersion effectively reduce three-phonon scattering processes by limiting the available phase space for energy and momentum conservation, thereby enhancing phonon transport efficiency (Fig. 4d-e). A similar mechanism due to degenerate acoustic phonons has also been reported in the *bcc* phases of metals W, Mo and Cr in Ref. 50. As a further comparison, we analyzed TiFe and ScCo with the same crystal structure as MnV but have larger frequency difference between acoustic and optical branches near *R* point, see Fig. 4b and Fig. 4d. These three materials exhibit similar group velocities across the entire Brillouin zone; however, their lifetimes differ by several orders of magnitude near the *R* point. As a result, the thermal conductivity contributions near the *R* point decrease significantly from MnV to TiFe and become negligible for ScCo (Fig. S12). This trend aligns with the increasing acoustic-optical frequency difference observed near the *R* point.

Electron-phonon scattering processes are known to hamper phonon transport in conventional metals. Interestingly, despite the metallic nature, the electron-phonon scattering in MnV only reduces its phonon thermal conductivity κ_{ph} by a factor of four as shown in Fig. 4f, contrasting a reduction of over a factor of ten observed in a few recently reported metallic compounds (e.g. TiN, HfN, NbC) that were also predicted to have high thermal conductivity with three-phonon processes.[51, 52] Electronic structure analysis reveals that the limited electron-phonon scattering originates from a sharp minimum of the electronic density of states (DOS) at the Fermi energy, see Fig. 4h and Fig. S9c-d. This electronic distribution leads to strong Mn–V bonds, as evidenced by the projected crystal orbital Hamilton population (pCOHP)[53, 54] which displays a rather distinct separation of bonding and anti-bonding states and a sharp drop of pCOHP values at the Fermi energy. This electronic configuration yields stiff bonds with high vibrational frequencies and maintains the metallic characteristic of the material, yet with moderate reduction of lattice thermal conductivity due to electron-phonon scattering. These characteristics lead to the unusually even balance between electronic and phononic heat transport. Such a feature may have significant implications for interconnect in semiconductor devices as it would reduce the thermal boundary resistance between metallic contacts and semiconducting layers.

7 Discussions

We conducted a large-scale search for high thermal conductivity materials using deep learning accelerated atomistic simulations to understand the limits of heat transport in solids and identify new thermal conductors. By systematically exploring the chemical and structural space of ordered inorganic crystals, we characterized 642,603 structures and computed lattice thermal conductivity for 236,574 dynamically stable ones. We confirm diamond to have the highest thermal conductivity among all searched structures and, most likely, in the overall space of bulk crystals, at ambient conditions. While not breaking the diamond limit, the search uncovered over 20 new high- κ candidates surpassing silicon with many in previously unexplored chemical and structural spaces, providing valuable references for advanced thermal management applications. Notably, we identified a class of metallic materials exhibiting both high electron- and phonon-mediated thermal conductivity, an exotic property previously not observed to the best of our knowledge. These findings not only expand the known landscape of thermal materials but also challenge conventional assumptions regarding phonon transport in metallic systems. Furthermore, this work offers the largest dataset to date for materials informatics and thermal management design.

Despite these findings, several limitations should be noted. Our search comprises two parts: an unbiased extensive sampling of simple crystals and an *ad hoc* selection of more complex structures. As a result, the upper bound for thermal conductivity is conclusively determined only for searched structures, although we expect this conclusion to hold more generally across the entire inorganic bulk crystalline space. The deep learning model, trained on large-scale density functional theory data, reproduces the overall energy landscape and achieves state-of-the-art accuracy in lattice thermal conductivity computations but still incurs an average error on the order of tens of $\text{W m}^{-1} \text{K}^{-1}$, potentially causing missed structures in the $150 \sim 300 \text{ W m}^{-1} \text{K}^{-1}$ range. Additionally, our screening, based on three-phonon scattering, may overestimate thermal conductivity, leading to discrepancies after incorporating all scattering processes. Lastly, while DFT using the PBE or LDA functional generally performs well, it has known limitations. Band gaps are systematically underestimated,[55–58] leading to the prediction that some small-gap semiconductors are metallic. The classification of materials in this paper into metals or non-metals in this paper are subject to this error, and as such the classification could be wrong in a small number of cases. Additionally, some of the structures are not on the convex hull, particularly those arising from the extensive random structure search, meaning that they are not predicted to be thermodynamically stable under the assumptions of the convex hull construction. It is likely that some structures will not be synthesizable or very difficult to synthesize, including those that depend on very specific ordering of species, the less energetically favorable polymorphs of well-studied material systems, and the unusual structures that are predicted

to only be stable under certain conditions, such as the theoretically predicted OsN₂ phase.[59] This is because dynamical stability is a necessary but not sufficient condition for synthesizability, and many dynamically stable structures cannot be synthesized. Despite this, the MatterK database provides a comprehensive collection of material candidates that can be used to guide further experimental efforts.

This work also highlights new opportunities in thermal conduction research enabled by deep learning. This work addresses the upper bound of heat conduction under ambient conditions, leveraging the insight that phonons are less prone to scattering in simple crystals, allowing a most exhaustive search to date with deep learning accelerated simulations. In contrast, determining the lower bound remains more complex,[60–65] as structurally intricate materials are likely to dominate, necessitating advanced search strategies such as generative models and others.[66, 67] Furthermore, the large-scale dataset generated in this study provides a valuable resource for future investigations. Systematic data mining may reveal new physical correlations and facilitate the discovery of materials optimized for diverse thermal management applications.

8 Methods

8.1 Chemical Search Space

The search pool is generated in-house through an AI-accelerated random structure search (RSS) and supplemented with data from the Materials Project (MP) database[68]. In this study, the terms “binary” and “ternary” systems are defined as follows. For binary systems, an exhaustive crystal structure search is conducted for compositions with up to four atoms per unit cell, considering elements with atomic number lower than 95, while excluding Group 18 elements, the highly radioactive element 61, 84–89 and 91. Given the computational cost and complexity of ternary systems, an exhaustive search across all possible ternary compositions is impractical. Since the lattice thermal conductivity of metals is normally low due to electron-phonon scattering and a large number of atoms in the unit cell leads to higher impact of three-phonon scattering, for ternary compounds we limit the RSS search to systems made of main-group elements 13–16 and fewer than 8 atoms per cell. This choice allows us to optimize search efficiency while capturing relevant chemical diversity. The RSS settings are the same as Ref.[41]. When an E_{hull} threshold of 0.2 eV/atom was later applied for identifying stable materials, the convex hull was constructed using the MP database v2022.10.28, while the E_{hull} values for the RSS structures were computed using MatterSim potentials.

8.2 Thermal conductivity workflow

All calculations were performed using the near first-principles foundational deep learning model, MatterSim. The computation of thermal conductivity was systematically carried out in four stages.

First, structural relaxation and filtering were conducted using the Fast Inertial Relaxation Engine (FIRE) algorithm to ensure that atomic forces remained below $0.001\text{ eV}/\text{\AA}$. Redundant and non-3D structures were subsequently excluded, with dimensionality identified using the Rank Determination Algorithm (RDA)[69] implemented in ASE.[70]

Following structural relaxation, phonon dispersion relations were computed using Phonopy.[71] Any system exhibiting imaginary frequencies above 10 cm^{-1} was discarded, as the presence of imaginary frequencies at 0 K indicates structural instability. Such instabilities typically require temperature-dependent renormalization of both second- and third-order force constants, often addressed through effective potential fitting or a self-consistent approach.[72–74] However, incorporating temperature-dependent effects into high-throughput screening would significantly increase computational cost and is therefore beyond the scope of this work.

For systems found to be dynamically stable, thermal conductivity calculations were performed using 3ph-BTE, as detailed in [subsection 8.3](#).

8.3 ML-accelerated force constants for BTE

The second-order interatomic force constants and phonon spectra are computed using Phonopy,[71] interfaced with the machine-learning potential MatterSim. The magnitude of finite displacements is set to 0.03 \AA .

The third-order force constants are computed using Phono3py,[71] maintaining the same supercell size and displacement magnitude as in the second-order calculations. No cutoff is imposed on the atomic distance when supercells are created for third-order force constants. The thermal conductivity is then solved using Phono3py within the Relaxation Time Approximation (RTA). To ensure convergence, the q-point mesh for Brillouin zone integration is set to six times the supercell size.

8.4 Predicting Mechanical Properties Using MatterSim

Elastic constants describe the stiffness of a material in response to small deformations (i.e., within the elastic regime). For isotropic materials, common moduli include Young's modulus E , shear modulus G , bulk modulus B , and Poisson's ratio ν . For anisotropic crystals, the elastic behavior is described by a full 6×6 symmetric matrix (expressed in Voigt notation) of independent elastic constants C_{ij} .

In the regime of small strains, Hooke's Law can be written as

$$\sigma_i = \sum_j C_{ij} \epsilon_j,$$

where σ_i are the stress components, ϵ_j are the strain components, and C_{ij} are the elastic constants. Furthermore, the change in energy due to strain can be expressed by a second-order Taylor expansion:

$$\Delta E = \frac{1}{2} V \sum_{i,j} C_{ij} \epsilon_i \epsilon_j,$$

which indicates that the elastic constants are essentially the second derivatives of the total energy with respect to strain. Since MatterSim provides the total energy, forces, and stress of a system, both the stress-strain method and the energy-strain method can, in principle, be used to compute the mechanical properties. However, the energy-strain method offers several advantages. For example, it is generally less sensitive to numerical noise in the calculated stresses and often yields more stable and convergent results, particularly when dealing with subtle energy differences. Moreover, the energy-strain method allows for a direct determination of the elastic constants as the second derivatives of the total energy with respect to strain. The energy-strain approach has been implemented in the VASPKIT software package[75]. To leverage this capability, we have developed an interface between MatterSim and VASPKIT, enabling efficient calculation of mechanical properties using the energy-strain method.

8.5 DFT validation

8.5.1 DFT 3ph

All force constants needed to solve the phonon BTE are calculated by projector-augmented plane wave method[76] as implemented in VASP,[77, 78] and the atomic displacement amplitude for finite displacement are set to 0.01 Å. The Generalized Gradient Approximation (GGA) Perdew-Burke-Ernzerhof (PBE) exchange-correlation functional[79] is used throughout the work unless stated otherwise. A 0.18 \AA^{-1} k points spacing is used to sample the first Brillouin Zone, and the plane-wave energy cut-off is set to 520 eV. We first perform structural optimization to ensure that the forces on the atoms in the system are less than 10^{-3} eV/\AA . Subsequently, we use the Phonopy[71] and ShengBTE[80] packages to calculate the second-order and third-order force constants, respectively. To ensure that the second-order and third-order force constants converge as much as possible, we require that the lattice constants along all three directions of the supercell are greater than 10 Å, and the number of atoms in the supercell is no less than 100. In the calculation of third-order force

constants, we selected the cut-off to the sixth nearest neighbor atom to balance computational efficiency and accuracy. For the calculation of Boltzmann transport equation, we test multiple q mesh points to obtain convergent lattice thermal conductivity values.

8.5.2 DFT 4ph

For the calculation of fourth-order force constants, the FourPhonon package[81] is used to generate displaced supercell and to compute the fourth-phonon interactions. We used a smaller supercell compared to the third-order force constant calculation, with one fewer unit cell in each direction, and the cut-off was set to the 2nd nearest neighbor atom.

8.5.3 DFT electron-phonon coupling

All electron-phonon related DFT calculation are performed using Quantum Espresso (QE) [82][83] package. The pseudopotential are used in pseudo-dojo[84] with Optimized norm-conserving Vanderbilt pseudopotentials[85] and GGA exchange-correlation functional. The k points to sample first Brillouin Zone are same as VASP used, and the plane-wave energy cut-off is set to 80 Ry. For lattice thermal conductivity limited by electron scattering, we employ the EPW [86][87] package along with QE to calculate phonon lifetime. And the modified ShengBTE package were used to include the phonon-electron scattering to calculate κ_{ph} . For electron thermal conductivity, we employ the PERTURBO[88] package based on maximally localized Wannier function[89] to calculate κ_{el} in dense k, q mesh to ensure convergence. For the Wannier interpolation used in EPW and PERTURBO, we carefully select the projector and energy window for each system to ensure that the Wannier function spread of each system is less than a lattice constant, and the interpolation values on the energy band near the Fermi surface and phonon spectrum are the same as those calculated by DFT.

8.5.4 Calculations of DOS and pCOHP

We calculated the electronic density state (DOS) and the projected crystal orbital Hamilton population (pCOHP) as shown in Fig. S9 using Lobster[53] package (version 5.11). Specifically, following a self-consistent field (SCF) calculation using VASP with a k -mesh density of $0.04 \times \pi \text{ \AA}^{-1}$ [75], the resulting output was processed with LOBSTER: The lobster input file was configured with an energy window from -10 to 10 eV relative to the Fermi energy (using **COHPStartEnergy** -10 and **COHPENDEnergy** 10) and defined the local basis by including s , p and d orbitals using the **includeOrbitals** command. To probe the atomic-resolved and orbital-resolved interactions between Mn and V, we generated the bonding interactions for all Mn-V pairs within a distance range of 1.0 to 3.0 \AA , employing the **cohpgenerator** command. The eDOS and pCOHP values are computed following this protocol.

9 Code Availability

The MatterSim model used in this work is already publicly available at: [MatterSim repository](#).

10 Acknowledgements

We thank Chris Bishop, Bin Shao, Ryota Tomioka, Jia Zhang, Karin Strauss for their invaluable support. We appreciate David Broido and David Cahill for insightful discussions. We acknowledge Bichlien Nguyen, Jake Smith for constructive feedbacks for the work; Deniz Gunceler and Maik Riechert for their support with our computational infrastructure; Jingyun Bai for improving the quality of the figures; Shoko Ueda, Peggy Dai and Roberto Sordillo for their instrumental management of the project. We are grateful to Kenji Takeda, Shruti Rajurkar, and others for their support in establishing external collaborations and overall study coordination. Additionally, HH thanks Wu Li, Yiyang Sun and Haibo Xiao for instructive discussions. HY thanks Cunzhi Zhang, Giulia Galli, Yi Xia, for their thoughtful suggestions during private discussions. ZC thanks Bohan Li, Wang-Yeuk Kong, Dylan Folkner, Kam-Tung Chan and Frank Cerasoli for fruitful discussions.

11 Author Contributions

JL, HY, ZL and HH conceived the study, JL, ZC, QW, HY, ZL, GL, SC, YZ, XL, JT, MT, YZ implemented the methods and workflows, JL, ZC, QW, HY, ZL, GL, SC, YZ, MT, CZ, AF performed experiments, CZ, AF, DZ, RP, MH, TX helped with the implementation of the methods and all authors participate discussions and wrote this manuscript. HH led the research.

Declarations

While drafting this manuscript, we utilized the language model GPT-4 to facilitate sentence-level composition and to ensure clarity and coherence.

References

- [1] Sanders, S. 125 questions: Exploration and discovery. *Science/AAAS Custom Publishing Office: Washington, DC, USA* (2021).
- [2] Ziman, J. M. *Electrons and phonons* (Oxford university press, 1960).
- [3] Phonons, P. T. O. E. M. Nanoscale energy transport and conversion a parallel treatment of electrons molecules phonons and photons mit pappalardo series in mechanical engineering by gang chen .

- [4] Cahill, D. G. *et al.* Nanoscale thermal transport. *Journal of applied physics* **93**, 793–818 (2003).
- [5] Moore, A. L. & Shi, L. Emerging challenges and materials for thermal management of electronics. *Materials today* **17**, 163–174 (2014).
- [6] Li, S. *et al.* High thermal conductivity in cubic boron arsenide crystals. *Science* **361**, 579–581 (2018).
- [7] Snyder, G. J. & Toberer, E. S. Complex thermoelectric materials. *Nature materials* **7**, 105–114 (2008).
- [8] Fourier, J. B. J. *Théorie analytique de la chaleur* (Firmin Didot Père et Fils, 1822).
- [9] Peierls, R. E. *Quantum theory of solids* (Clarendon Press, 1996).
- [10] Callaway, J. Model for lattice thermal conductivity at low temperatures. *Physical Review* **113**, 1046 (1959).
- [11] Peierls, R. Zur kinetischen theorie der wärmeleitung in kristallen. *Annalen der Physik* **395**, 1055–1101 (1929).
- [12] Olson, J. *et al.* Thermal conductivity of diamond between 170 and 1200 k and the isotope effect. *Physical Review B* **47**, 14850 (1993).
- [13] Wei, L., Kuo, P., Thomas, R., Anthony, T. & Banholzer, W. Thermal conductivity of isotopically modified single crystal diamond. *Physical review letters* **70**, 3764 (1993).
- [14] Broido, D. A., Malorny, M., Birner, G., Mingo, N. & Stewart, D. Intrinsic lattice thermal conductivity of semiconductors from first principles. *Applied Physics Letters* **91** (2007).
- [15] Marcolongo, A., Umari, P. & Baroni, S. Microscopic theory and quantum simulation of atomic heat transport. *Nature Physics* **12**, 80–84 (2016).
- [16] Carbogno, C., Ramprasad, R. & Scheffler, M. Ab initio green-kubo approach for the thermal conductivity of solids. *Physical review letters* **118**, 175901 (2017).
- [17] Puligheddu, M., Gygi, F. & Galli, G. First-principles simulations of heat transport. *Physical Review Materials* **1**, 060802 (2017).
- [18] Lindsay, L., Broido, D. & Reinecke, T. First-principles determination of ultrahigh thermal conductivity of boron arsenide: a competitor for diamond? *Physical review letters* **111**, 025901 (2013).

- [19] Feng, T., Lindsay, L. & Ruan, X. Four-phonon scattering significantly reduces intrinsic thermal conductivity of solids. *Physical Review B* **96**, 161201 (2017).
- [20] Yang, X., Feng, T., Li, J. & Ruan, X. Stronger role of four-phonon scattering than three-phonon scattering in thermal conductivity of iii-v semiconductors at room temperature. *Physical Review B* **100**, 245203 (2019).
- [21] Kundu, A., Ma, J., Carrete, J., Madsen, G. & Li, W. Anomalously large lattice thermal conductivity in metallic tungsten carbide and its origin in the electronic structure. *Materials Today Physics* **13**, 100214 (2020).
- [22] Kundu, A. *et al.* Ultrahigh thermal conductivity of θ -phase tantalum nitride. *Physical Review Letters* **126**, 115901 (2021).
- [23] Ward, A., Broido, D., Stewart, D. A. & Deinzer, G. Ab initio theory of the lattice thermal conductivity in diamond. *Physical Review B* **80**, 125203 (2009).
- [24] Xia, Y. *et al.* High-throughput study of lattice thermal conductivity in binary rocksalt and zinc blende compounds including higher-order anharmonicity. *Physical Review X* **10**, 041029 (2020).
- [25] van Roekeghem, A., Carrete, J., Oses, C., Curtarolo, S. & Mingo, N. High-throughput computation of thermal conductivity of high-temperature solid phases: the case of oxide and fluoride perovskites. *Physical Review X* **6**, 041061 (2016).
- [26] Kang, J. S., Li, M., Wu, H., Nguyen, H. & Hu, Y. Experimental observation of high thermal conductivity in boron arsenide. *Science* **361**, 575–578 (2018).
- [27] Tian, F. *et al.* Unusual high thermal conductivity in boron arsenide bulk crystals. *Science* **361**, 582–585 (2018).
- [28] Lv, B. *et al.* Experimental study of the proposed super-thermal-conductor: Bas. *Applied Physics Letters* **106** (2015).
- [29] Zheng, Q. *et al.* Antisite pairs suppress the thermal conductivity of bas. *Physical review letters* **121**, 105901 (2018).
- [30] Togo, A., Chaput, L. & Tanaka, I. Distributions of phonon lifetimes in brillouin zones. *Physical review B* **91**, 094306 (2015).
- [31] Knoop, F., Scheffler, M. & Carbogno, C. Ab initio green-kubo simulations of heat transport in solids: method and implementation. *Physical Review B* **107**, 224304 (2023).

- [32] Knoop, F., Purcell, T. A., Scheffler, M. & Carbogno, C. Anharmonicity in thermal insulators: An analysis from first principles. *Physical Review Letters* **130**, 236301 (2023).
- [33] Zhang, A. & Li, Y. Thermal conductivity of aluminum alloys—a review. *Materials* **16**, 2972 (2023).
- [34] Qin, G. *et al.* High-throughput computational evaluation of lattice thermal conductivity using an optimized slack model. *Materials Advances* **3**, 6826–6830 (2022).
- [35] Juneja, R., Yumnam, G., Satsangi, S. & Singh, A. K. Coupling the high-throughput property map to machine learning for predicting lattice thermal conductivity. *Chemistry of Materials* **31**, 5145–5151 (2019).
- [36] Toher, C. *et al.* High-throughput computational screening of thermal conductivity, debye temperature, and grüneisen parameter using a quasiharmonic debye model. *Physical Review B* **90**, 174107 (2014).
- [37] Póta, B., Ahlawat, P., Csányi, G. & Simoncelli, M. Thermal conductivity predictions with foundation atomistic models. *arXiv preprint arXiv:2408.00755* (2024).
- [38] Slack, G. A. Nonmetallic crystals with high thermal conductivity. *Journal of Physics and Chemistry of Solids* **34**, 321–335 (1973).
- [39] Pickard, C. J. & Needs, R. High-pressure phases of silane. *Physical review letters* **97**, 045504 (2006).
- [40] Pickard, C. J. & Needs, R. Ab initio random structure searching. *Journal of Physics: Condensed Matter* **23**, 053201 (2011).
- [41] Yang, H. *et al.* Mattersim: A deep learning atomistic model across elements, temperatures and pressures. *arXiv preprint arXiv:2405.04967* (2024).
- [42] Hohenberg, P. & Kohn, W. Inhomogeneous electron gas. *Physical review* **136**, B864 (1964).
- [43] Kohn, W. & Sham, L. J. Self-consistent equations including exchange and correlation effects. *Physical review* **140**, A1133 (1965).
- [44] Lindsay, L. First principles peierls-boltzmann phonon thermal transport: a topical review. *Nanoscale and Microscale Thermophysical Engineering* **20**, 67–84 (2016).

- [45] Loew, A., Sun, D., Wang, H.-C., Botti, S. & Marques, M. A. Universal machine learning interatomic potentials are ready for phonons. *arXiv preprint arXiv:2412.16551* (2024).
- [46] Deng, B. *et al.* Systematic softening in universal machine learning interatomic potentials. *npj Computational Materials* **11**, 1–9 (2025).
- [47] Riebesell, J. *et al.* Matbench discovery—a framework to evaluate machine learning crystal stability predictions. *arXiv preprint arXiv:2308.14920* (2023).
- [48] Lian, C.-S., Wang, X.-Q. & Wang, J.-T. Hydrogenated k4 carbon: A new stable cubic gauche structure of carbon hydride. *The Journal of Chemical Physics* **138** (2013).
- [49] Liu, S., Zhang, X. & Tang, D. First-principles study of the thermal transport properties of superconducting nbn (2023).
- [50] Chen, Y., Ma, J., Wen, S. & Li, W. Body-centered-cubic structure and weak anharmonic phonon scattering in tungsten. *npj Computational Materials* **5**, 98 (2019).
- [51] Li, S. *et al.* Anomalous thermal transport in metallic transition-metal nitrides originated from strong electron–phonon interactions. *Materials Today Physics* **15**, 100256 (2020).
- [52] Li, C., Ravichandran, N. K., Lindsay, L. & Broido, D. Fermi surface nesting and phonon frequency gap drive anomalous thermal transport. *Physical review letters* **121**, 175901 (2018).
- [53] Deringer, V. L., Tchougréeff, A. L. & Dronskowski, R. Crystal orbital hamilton population (cohp) analysis as projected from plane-wave basis sets. *The journal of physical chemistry A* **115**, 5461–5466 (2011).
- [54] Nelson, R., Ertural, C., Müller, P. C. & Dronskowski, R. in *3.07 - chemical bonding with plane waves* Third edition edn, (eds Reedijk, J. & Poeppelmeier, K. R.) *Comprehensive Inorganic Chemistry III (Third Edition)* 141–201 (Elsevier, Oxford, 2023). URL <https://www.sciencedirect.com/science/article/pii/B9780128231449001205>.
- [55] Grumet, M., Liu, P., Kaltak, M., Klimeš, J. & Kresse, G. Beyond the quasiparticle approximation: Fully self-consistent gw calculations. *Physical Review B* **98**, 155143 (2018).
- [56] Govoni, M. & Galli, G. Gw100: comparison of methods and accuracy of results obtained with the west code. *Journal of chemical theory and computation* **14**, 1895–1909 (2018).
- [57] Nguyen, N. L., Colonna, N., Ferretti, A. & Marzari, N. Koopmans-compliant spectral functionals for extended systems. *Physical Review X* **8**, 021051 (2018).

- [58] Yang, H., Govoni, M. & Galli, G. Improving the efficiency of gw calculations with approximate spectral decompositions of dielectric matrices. *The Journal of Chemical Physics* **151** (2019).
- [59] Li, Y. *et al.* Twofold coordinated ground-state and eightfold high-pressure phases of heavy transition metal nitrides mn2 ($m = \text{os, ir, ru, and rh}$). *Inorganic Chemistry* **48**, 9904–9909 (2009). URL <http://dx.doi.org/10.1021/ic9014702>.
- [60] Cahill, D. G., Watson, S. K. & Pohl, R. O. Lower limit to the thermal conductivity of disordered crystals. *Physical Review B* **46**, 6131 (1992).
- [61] Chiritescu, C. *et al.* Ultralow thermal conductivity in disordered, layered wse2 crystals. *Science* **315**, 351–353 (2007).
- [62] Xia, Y. *et al.* A unified understanding of minimum lattice thermal conductivity. *Proceedings of the National Academy of Sciences* **120**, e2302541120 (2023).
- [63] Zhao, L.-D. *et al.* Ultralow thermal conductivity and high thermoelectric figure of merit in snse crystals. *nature* **508**, 373–377 (2014).
- [64] Mukhopadhyay, S. *et al.* Two-channel model for ultralow thermal conductivity of crystalline tl3vse4. *Science* **360**, 1455–1458 (2018).
- [65] Gibson, Q. D. *et al.* Low thermal conductivity in a modular inorganic material with bonding anisotropy and mismatch. *Science* **373**, 1017–1022 (2021).
- [66] Zeni, C. *et al.* A generative model for inorganic materials design. *Nature* 1–3 (2025).
- [67] Pal, K., Park, C. W., Xia, Y., Shen, J. & Wolverton, C. Scale-invariant machine-learning model accelerates the discovery of quaternary chalcogenides with ultralow lattice thermal conductivity. *npj Computational Materials* **8**, 48 (2022).
- [68] Jain, A. *et al.* Commentary: The materials project: A materials genome approach to accelerating materials innovation. *APL materials* **1** (2013).
- [69] Larsen, P. M., Pandey, M., Strange, M. & Jacobsen, K. W. Definition of a scoring parameter to identify low-dimensional materials components. *Physical Review Materials* **3**, 034003 (2019).
- [70] Larsen, A. H. *et al.* The atomic simulation environment—a python library for working with atoms. *Journal of Physics: Condensed Matter* **29**, 273002 (2017).

- [71] Togo, A. First-principles phonon calculations with phonopy and phono3py. *J. Phys. Soc. Jpn.* **92**, 012001 (2023).
- [72] Errea, I., Calandra, M. & Mauri, F. Anharmonic free energies and phonon dispersions from the stochastic self-consistent harmonic approximation: Application to platinum and palladium hydrides. *Physical Review B* **89**, 064302 (2014).
- [73] Knoop, F. *et al.* Tdep: Temperature dependent effective potentials. *Journal of Open Source Software* **9** (2024).
- [74] Folkner, D. A., Chen, Z., Barbalinardo, G., Knoop, F. & Donadio, D. Elastic moduli and thermal conductivity of quantum materials at finite temperature. *Journal of Applied Physics* **136** (2024).
- [75] Wang, V., Xu, N., Liu, J.-C., Tang, G. & Geng, W.-T. Vasptkit: A user-friendly interface facilitating high-throughput computing and analysis using vasp code. *Computer Physics Communications* **267**, 108033 (2021).
- [76] Blöchl, P. E. Projector augmented-wave method. *Phys. Rev. B* **50**, 17953–17979 (1994). URL <https://link.aps.org/doi/10.1103/PhysRevB.50.17953>.
- [77] Kresse, G. & Furthmüller, J. Efficient iterative schemes for ab initio total-energy calculations using a plane-wave basis set. *Phys. Rev. B* **54**, 11169–11186 (1996). URL <https://link.aps.org/doi/10.1103/PhysRevB.54.11169>.
- [78] Kresse, G. & Joubert, D. From ultrasoft pseudopotentials to the projector augmented-wave method. *Phys. Rev. B* **59**, 1758–1775 (1999). URL <https://link.aps.org/doi/10.1103/PhysRevB.59.1758>.
- [79] Perdew, J. P., Burke, K. & Ernzerhof, M. Generalized gradient approximation made simple. *Physical review letters* **77**, 3865 (1996).
- [80] Li, W., Carrete, J., A. Katcho, N. & Mingo, N. Shengbte: A solver of the boltzmann transport equation for phonons. *Computer Physics Communications* **185**, 1747–1758 (2014). URL <https://www.sciencedirect.com/science/article/pii/S0010465514000484>.
- [81] Han, Z., Yang, X., Li, W., Feng, T. & Ruan, X. Fourphonon: An extension module to shengbte for computing four-phonon scattering rates and thermal conductivity. *Computer Physics Communications* **270**, 108179 (2022). URL <https://www.sciencedirect.com/science/article/pii/S0010465521002915>.

- [82] Giannozzi, P. *et al.* Quantum espresso: a modular and open-source software project for quantum simulations of materials. *Journal of physics: Condensed matter* **21**, 395502 (2009).
- [83] Giannozzi, P. *et al.* Advanced capabilities for materials modelling with quantum espresso. *Journal of physics: Condensed matter* **29**, 465901 (2017).
- [84] van Setten, M. *et al.* The pseudodojo: Training and grading a 85 element optimized norm-conserving pseudopotential table. *Computer Physics Communications* **226**, 39–54 (2018). URL <https://www.sciencedirect.com/science/article/pii/S0010465518300250>.
- [85] Hamann, D. Optimized norm-conserving vanderbilt pseudopotentials. *Physical Review B—Condensed Matter and Materials Physics* **88**, 085117 (2013).
- [86] Giustino, F., Cohen, M. L. & Louie, S. G. Electron-phonon interaction using wannier functions. *Phys. Rev. B* **76**, 165108 (2007). URL <https://link.aps.org/doi/10.1103/PhysRevB.76.165108>.
- [87] Lee, H. *et al.* Electron-phonon physics from first principles using the epw code. *npj Computational Materials* **9**, 156 (2023).
- [88] Zhou, J.-J. *et al.* Perturbo: A software package for ab initio electron–phonon interactions, charge transport and ultrafast dynamics. *Computer Physics Communications* **264**, 107970 (2021).
- [89] Pizzi, G. *et al.* Wannier90 as a community code: new features and applications. *Journal of Physics: Condensed Matter* **32**, 165902 (2020). URL <https://doi.org/10.1088%2F1361-648x%2Fab51ff>.

Supplementary Information: Probing the Limit of Heat Transfer in Inorganic Crystals with Deep Learning

Jielan Li^{1†}, Zekun Chen^{1†}, Qian Wang^{1†}, Han Yang^{1*†}, Ziheng Lu^{1*†}, Guanzhi Li¹, Shuizhou Chen¹, Yu Zhu¹, Xixian Liu¹, Junfu Tan¹, Mingfa Tang¹, Yichi Zhou¹, Claudio Zeni¹, Andrew Fowler¹, Daniel Zügner¹, Robert Pinsler¹, Matthew Horton¹, Tian Xie¹, Tie-Yan Liu¹, Haiguang Liu¹, Tao Qin¹, Bing Lv², Davide Donadio^{3*}, Hongxia Hao^{1*}

¹Microsoft Research AI for Science.

²Department of Physics, University of Texas at Dallas, Richardson, TX 75080, USA.

³Department of Chemistry, University of California Davis, Davis, CA 95616, USA.

*Corresponding author(s). E-mail(s): hanyang@microsoft.com;

zihenglu@microsoft.com; ddonadio@ucdavis.edu; hongxiahao@microsoft.com;

†These authors contributed equally to this work.

In addition to this supporting information document, some other supplementary files will be attached:
a) Unconfirmed high thermal conductors b) MatterK database c) All ternary compounds and the corresponding highest binary compounds. d) DFT verification setting.

Contents

S1 Search space	2
S1.1 Search space definition	2
S1.2 Thermal conductivity distribution from Materials Project	2
S2 Benchmarks	4
S2.1 Three-Phonon Boltzmann Transport Equation	4
S2.2 Elastic Moduli Predictions from MatterSim	5
S3 MatterK, database	13
S3.1 The database	13
S3.2 Thermal conductivity phase diagram for RSS B-C-N chemical system and beyond . . .	13
S3.3 Revisit the Slack's rule	14

S4 Thermal conductivity distributions	15
S5 High thermal conductors	17
S6 Metals with novel thermal transport mechanism	21
S6.1 Detailed analysis for MnV, TiFe & ScCo	21

S1 Search space

S1.1 Search space definition

Fig. S1 illustrates the construction details of the chemical search space and their contributions to the final MatterK database where high thermal conductors most likely reside. The in-house designed target search space resulted in $> 6M$ unique crystal structure entries, which is too large to be fully screened using MatterSim-BTE. Here we chose to conduct an extensive screening using MatterSim-BTE for a subset of the materials, i.e., binary and ternary systems with up to 4 atoms in the unit cell and $E_{\text{hull}} \leq 0.2$ eV/atom, aiming to effectively traverse the local energy minima and explore the heat limit for stable materials under ambient conditions. For the other subsets, some ad-hoc screening rules/constraints are applied to select the more relevant material entries followed by MatterSim-BTE screening. The few subsets are: (1) binary and ternary materials composed of either 6 or 8 atoms in the unit cell with $E_{\text{hull}} \leq 0.2$ eV/atom, with/out filtered by bulk modulus higher than 100GPa; (2) binary materials composed of up-to-8 atoms per unit cell with $E_{\text{hull}} > 0.2$ eV/atom, selecting the lowest-energy entry for each unique composition and unique symmetry; (3) ternary materials composed of up-to-8 atoms in the unit cell with $E_{\text{hull}} > 0.2$ eV/atom, selecting the ten lowest-energy entries for each unique composition; (4) BCN system for all E_{hull} ranges. (5) Materials Project database with up-to-16 atoms per unit cell.

S1.2 Thermal conductivity distribution from Materials Project

To validate the criteria used in defining the search space as above, we screened the Materials Project[1] database with minimal bias (up-to-16 atoms per unit cell) using MatterSim screening, where 3ph-BTE computation is conducted for dynamically stable materials after geometry optimization. The results indicate that 95% of materials with thermal conductivity exceeding that of silicon ($145 \text{ W m}^{-1} \text{ K}^{-1}$) belong to up-to-ternary chemical systems with no more than eight atoms per unit cell (**Fig. S2**). Notably, no materials meeting this thermal conductivity threshold were found in systems with five or seven atoms per unit cell, and the candidates that have more than four atoms in the unit cell

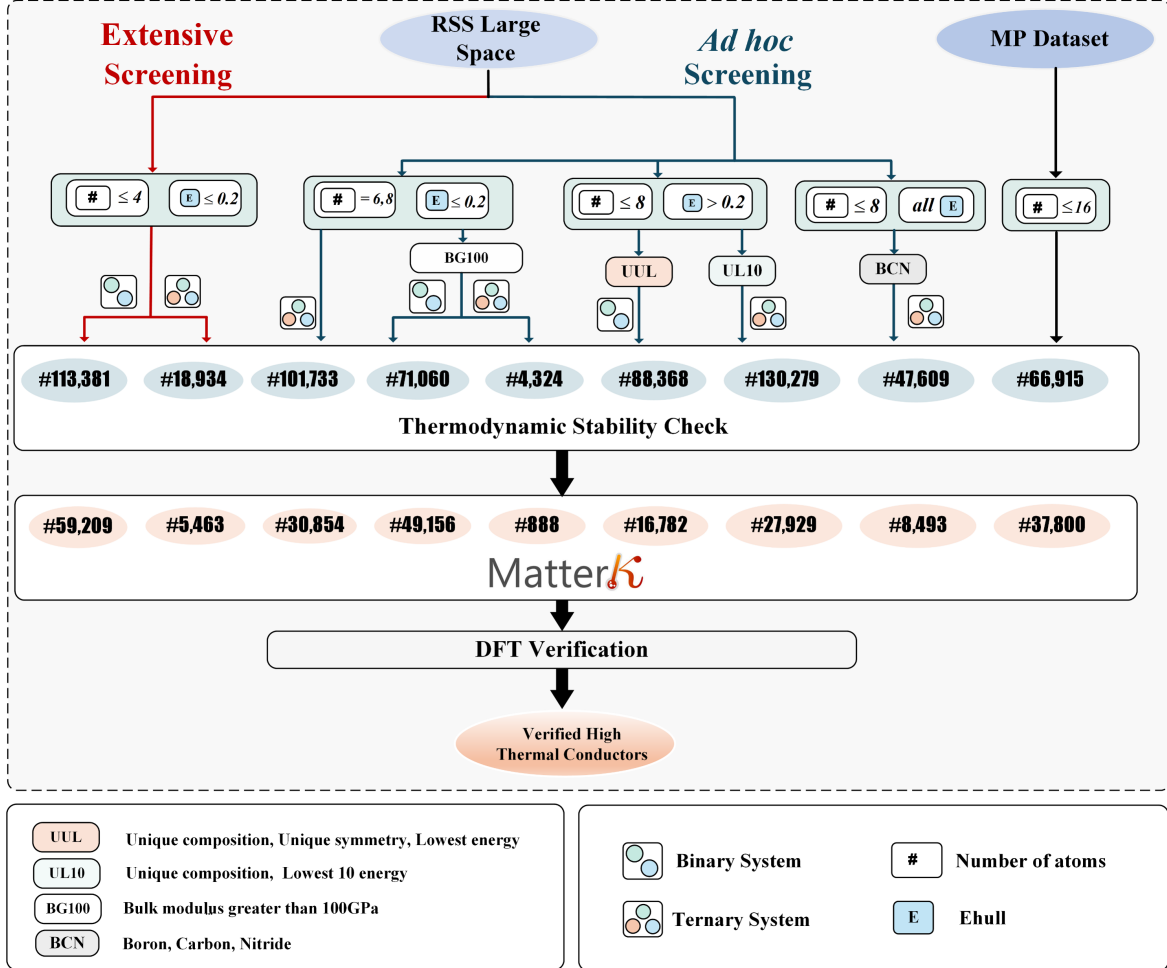


Fig. S1: Detailed illustration of the chemical search space generated from random structure search (RSS) and Materials Project (MP) and selection rules designed to identify regions where high thermal conductors are most likely to be found. The final selected structures undergo thermodynamic stability check followed by MatterSim-BTE calculations, forming the MatterK database. The number in blue circles indicate the structure counts from each category that will go through the thermodynamic stability check through harmonic lattice dynamics. The number in orange circles indicate the structure counts from each category that go through MatterSim-BTE calculator and contribute to the MatterK database. The selection rules are listed in the bottom left.

but possess thermal conductivity exceeding $500 \text{ W m}^{-1} \text{ K}^{-1}$ all belong to the B-C-N chemical system. These findings validate our RSS space design strategy, which focuses on binary and ternary systems with up to eight atoms per unit cell while excluding five- and seven-atom configurations, and MatterSim-BTE screening focus more on simple structures with at most four atoms per unit cell. It's worth noting the high thermal conductivity material identified with 16 atoms per unit cell is a diamond-like carbon structure. We anticipate that similar high thermal conductivity materials may exist in systems with larger unit cells, such as 32 or 64 atoms; however, exploring these systems is beyond the scope of this work.

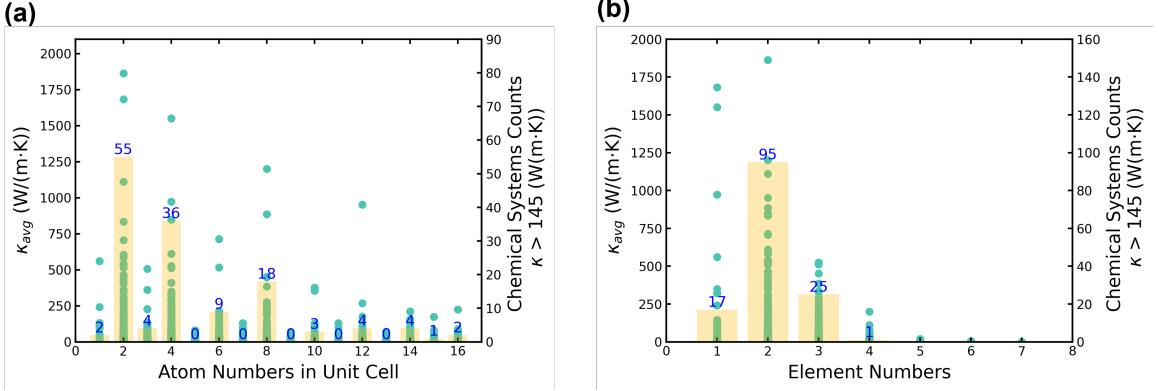


Fig. S2: Lattice thermal conductivity κ distribution analysis for Materials Project database screened using MatterSim-BTE. (a) κ vs number of atoms in unit cell. (b) κ vs number of elements in unit cell. The dots represent the distribution of all structures within each category, while the bars and numbers indicate the high thermal conductivity candidates ($> 145 \text{ W m}^{-1} \text{ K}^{-1}$) in that category.

S2 Benchmarks

S2.1 Three-Phonon Boltzmann Transport Equation

Here we proceed with a thorough and systematic benchmark on the κ predictions when coupling MatterSim with the three-phonon Boltzmann transport equation (3ph-BTE). BTE captures nuclear quantum effects and is much more computationally affordable compared to equilibrium molecular dynamics (EMD). Thus, BTE has been the method of choice for materials with high thermal conductivity[2–4]. In this work, we compared a set of 120 materials, of which their κ were either probed experimentally or validated with first-principle based BTE calculations[5–31]. The raw data for the benchmark plot in Fig. 2c is shown in Table S3.

To evaluate κ predictions across different orders of magnitude, we report a few error metrics here.

(1) Average factor difference (AFD). In the context of thermal transport, AFD can be defined as follow:

$$10^x; x = \frac{1}{N} \sum_i^N |\log_{10}(\kappa_{\ell,i}) - \log_{10}(\kappa_{ref,i})|, \quad (1)$$

where N represents the number of benchmarking systems, and κ denotes the MatterSim predictions, which are derived from BTE. Several studies have adopted the use of AFD in high-throughput screening of κ using end-to-end models, where the ground truth labels are sourced from experimental measurements[32–34].

(2) Symmetric Relative Error(SRE)

$$\text{SRE}[\kappa] = \frac{1}{N} \sum_i^N 2 \frac{|\kappa_{\ell,i} - \kappa_{ref,i}|}{\kappa_{\ell,i} + \kappa_{ref,i}}. \quad (2)$$

Table S1: Performance of M3GNet-MP, CHGNet, Mattersim, MACE-MPA, OMAT24, SevenNet, GRACE-2L-OMA and MACE-OMAT, on prediction of κ on the in-house κ dataset listed in [Table S3](#).

MAE of	M3GNet-MP	CHGNet	Mattersim	MACE-MPA-0	OMAT24	SevenNet	GRACE-2L-OMA	MACE-OMAT
SRE[κ]	1.33	1.81	0.36	0.35	1.89	0.69	0.20	0.22
MAE[κ] ($\text{W m}^{-1} \text{K}^{-1}$)	105.69	118.93	42.68	132.55	1.3e5	76.89	41.74	93.94
AFD[κ]	10.78	161.37	1.52	1.48	2.7e4	2.56	2.98	2.41
MAPE[κ] (%)	77.37	94.43	39.29	50.30	849498.29	50.41	48.76	42.53

Table S2: Performance of M3GNet-MP, CHGNet, Mattersim, MACE-MPA, OMAT24, SevenNet, GRACE-2L-OMA and MACE-OMAT, on prediction of κ on the **high** thermal conductivity materials (in-house κ dataset with κ_{ref} higher than $100 \text{ W m}^{-1} \text{K}^{-1}$) listed in [Table S3](#).

MAE of	M3GNet-MP	CHGNet	Mattersim	MACE-MPA-0	OMAT24	SevenNet	GRACE-2L-OMA	MACE-OMAT
SRE[κ]	1.59	1.95	0.37	0.52	1.93	0.88	0.38	0.33
MAE[κ] ($\text{W m}^{-1} \text{K}^{-1}$)	457.85	510.03	187.86	624.19	1.9e4	343.20	191.17	443.28
AFD[κ]	24.03	604.81	1.57	1.89	1124434.33	3.29	8.28	5.93
MAPE[κ] (%)	86.06	98.51	27.95	71.82	6605.99	59.66	28.16	41.03

(3) mean absolute error(MAE) and mean absolute percentage error(MAPE)

$$\text{MAE}[\kappa] = \frac{1}{N} \sum_i^N |\kappa_{\ell,i} - \kappa_{ref,i}| \quad (3)$$

$$\text{MPAE}[\kappa] = \frac{1}{N} \sum_i^N \frac{|\kappa_{\ell,i} - \kappa_{ref,i}|}{\kappa_{ref,i}} \quad (4)$$

S2.2 Elastic Moduli Predictions from MatterSim

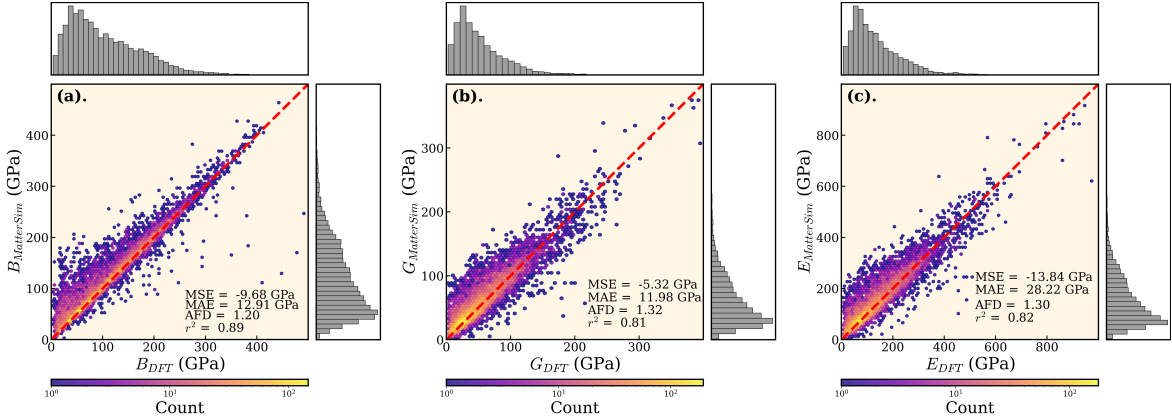


Fig. S3: Prediction performance from MatterSim on various elastic properties: (a) Bulk modulus (B), (b) shear modulus (G), and (C) Young's modulus (E) in comparison to DFT calculations. DFT data is adopted from Material project[35, 36].

Table S3: Summary of BTE benchmark. Rank of materials is determined based on $\kappa_{MatterSim}^{BTE}$ predicted under RTA. DFT-based BTE reference calculations performed in-house is indicated as **This work**. "h-" notation implies the hexagonal shape of the unit cell. κ values shown in the table are $W\ m^{-1}\ K^{-1}$. RS, ZB, and WZ represent Rock-salt, Zinc-blende, and Wurtzite, respectively.

Rank	Materials	mp-id	$\kappa_{MatterSim}^{BTE}$	κ_{ref}	κ_{ref}	Type	Source
1	C	mp-66	1683	1957		Theory	[37]
2	BN	mp-1639	1109	1170		Theory	[21]
3	BAs	mp-10044	850.1	1680.162		Theory	This work
4	h-BN	mp-2653	846	927		Theory	[21]
5	GeC	mp-1002164	548.4	1099.3		Theory	[20]
6	BC ₂ N	mp-30148	525	853		Theory	[37]
7	BSb	mp-997618	472.7	537.2		Theory	This work
8	SiC	mp-8062	465	415		Theory	[21]
9	BC ₂ N	mp-629458	451.6	804		Theory	[37]
10	h-SiC	mp-7140	377	375		Theory	[21]
11	BeO	mp-1778	352	358		Theory	[21]
12	BP	mp-1479	275.4	414.7		Theory	[27]
13	h-BeO	mp-2542	273.5	292		Theory	[21]
14	AlN	mp-1700	232.6	212		Theory	[21]
15	h-GaN	mp-804	206.7	225.5		Theory	[21]
16	GaN	mp-830	199.6	231		Theory	[21]
17	GaP	mp-2490	178.3	118.1		Theory	[27]
18	BeTe	mp-252	173.7	253.5		Theory	This work
19	BeSe	mp-1541	168	226.7		Theory	This work
20	Si	mp-149	145.1	145		Theory	[38]
21	BeS	mp-442	139	157		Theory	[21]
22	C ₃ N ₄	mp-2852	133.6	229		Theory	[37]
23	pseudo-C ₃ N ₄	mp-571653	128.6	262		Theory	[37]
24	AlSb	mp-2624	127	86.6		Theory	[27]
25	h-GaP	mp-8882	103.1	97.4		Theory	[21]
26	Be ₂ C	mp-1569	94.6	112.0		Theory	[37]
27	InN	mp-20411	77.8	95.4		Theory	[21]
28	InP	mp-20351	74.4	89.1		Theory	[27]

Continued on next page

Table S3: (continued)

Rank	Materials	mp-id	$\kappa_{MatterSim}^{BTE}$	κ_{ref}	κ_{ref}	Type	Source
29	AlP	mp-1550	71.9	83	Theory	[21]	
30	ZnO	mp-1986	66.4	58.2	Theory	[21]	
31	h-InP	mp-966800	61.9	67.2	Theory	[21]	
32	h-AlP	mp-8880	60.2	73.1	Theory	[21]	
33	h-ZnO	mp-2133	52.8	52.4	Theory	[21]	
34	MgO	mp-1265	51.5	55.4	Theory	[27]	
35	Ge	mp-32	51.5	65	Experiment	[15]	
36	ZnS	mp-10695	50.1	41.8	Theory	[27]	
37	ZnSe	mp-1190	31.2	19.0	Theory	[27]	
38	GaAs	mp-2534	30.6	31.8	Theory	[21]	
39	MgSe	mp-13031	30.4	20	Theory	[31]	
40	NiO	mp-19009	27.2	30	Experiment	[5]	
41	MgTe	mp-13033	26.5	15.7	Theory	[21]	
42	GaSb	mp-1156	26.1	32.5	Theory	[27]	
43	InAs	mp-20305	25.9	27.9	Theory	[27]	
44	CaS	mp-1672	24.2	33.7	Theory	[29]	
45	CaO	mp-2605	23.0	23.2	Theory	[27]	
46	h-GaAs	mp-8883	22.6	27.3	Theory	[21]	
47	h-ZnSe	mp-380	20.7	15.2	Theory	[21]	
48	TiCoSb	mp-5967	19.8	12	Experiment	[14]	
49	MgS	mp-1315	19.5	22.59	Theory	[29]	
50	LiSiB	mp-1100392	18.5	23.45	Theory	[30]	
51	h-InAs	mp-1007652	18.5	17.7	Theory	[21]	
52	NaF	mp-682	18.35	23.5	Theory	[27]	
53	VFeSb	mp-567636	17.1	13.0	Experiment	[13]	
54	Li ₂ O	mp-1960	16.7	11.0	Experiment	[9]	
55	h-CdS	mp-672	16.35	19	Theory	[21]	
56	TiNiSn	mp-924130	15.8	9.3	Experiment	[12]	
57	InSb	mp-20012	14.8	20.0	Experiment	[15]	
58	h-ZnTe	mp-8884	14.6	15.0	Theory	[21]	

Continued on next page

Table S3: (continued)

Rank	Materials	mp-id	$\kappa_{MatterSim}^{BTE}$	κ_{ref}	κ_{ref}	Type	Source
59	CdSe	mp-2691	14.5	10.3	Theory	[21]	
60	SrSe	mp-2758	14.3	19.36	Theory	[29]	
61	ThO ₂	mp-643	12.7	14.0	Experiment	[16]	
62	CaSe	mp-1415	12.4	15.56	Theory	[29]	
63	CeO ₂	mp-20194	12.4	10.8	Experiment	[39]	
64	CdS	mp-2469	12.4	21.3	Theory	[21]	
65	SrSiO ₃	mp-1017439	11.9	10.1	Experiment	[19]	
66	NaH	mp-23870	11.9	15.41	Theory	[24]	
67	LiH	mp-23703	11.7	14.9	Theory	[27]	
68	LiF	mp-1138	11.5	13.3	Theory	[27]	
69	h-CdSe	mp-1070	11.4	9.22	Theory	[21]	
70	HfSnPd	mp-11869	10.75	9.32	Theory	[30]	
71	Mg ₂ Si	mp-1367	9.25	8.2	Experiment	[6, 7]	
72	h-CuH	mp-24093	9.23	7.32	Theory	[21]	
73	SrO	mp-2472	9.05	10.0	Theory	[27]	
74	CaTe	mp-1519	8.91	10.13	Theory	[29]	
75	MgSe	mp-10760	8.63	10.98	Theory	[29]	
76	CaF ₂	mp-2741	8.61	9.76	Theory	[27]	
77	CdTe	mp-406	8.16	7.55	Theory	[27]	
78	KMgF ₃	mp-3448	8.04	8.25	Theory	[23]	
79	SrS	mp-1087	7.86	12.81	Theory	[29]	
80	CoSb ₃	mp-1317	7.65	10.0	Experiment	[11]	
81	HgTe	mp-2730	7.61	4.62	Theory	This work	
82	h-CuI	mp-569346	7.54	6.51	Theory	[21]	
83	Sb ₃ Ir	mp-1239	7.34	16.0	Experiment	[18]	
84	h-CdTe	mp-12779	7.09	5.35	Theory	[21]	
85	NbCoSn	mp-1094088	6.93	12.23	Theory	[30]	
86	Mg ₂ Ge	mp-408	6.73	9.3	Experiment	[6, 7]	
87	Mg ₂ Pb	mp-20724	6.36	18.0	Experiment	[8]	
88	NaCl	mp-22862	6.29	8.45	Theory	[27]	

Continued on next page

Table S3: (continued)

Rank	Materials	mp-id	$\kappa_{MatterSim}^{BTE}$	κ_{ref}	κ_{ref}	Type	Source
89	SrTe	mp-1958	6.14	10.16	Theory	[29]	
90	MgTe	mp-1008786	5.9	4.45	Theory	[29]	
91	ZnO	mp-2229	5.79	6.7	Theory	This work	
92	KCl	mp-23193	5.36	7.75	Theory	[27]	
93	RbMgF ₃	mp-8402	4.64	4.54	Theory	[23]	
94	KF	mp-463	4.61	6.5	Theory	[27]	
95	GeTe	mp-938	4.56	2.34	Theory	[40]	
96	Mg ₂ Sn	mp-2343	4.553	7.1	Experiment	[6, 7]	
97	BaS	mp-1500	4.44	3.07	Theory	This work	
98	SrF ₂	mp-981	4.06	9.035	Experiment	[17]	
99	CsCaF ₃	mp-7104	3.05	3.03	Theory	[23]	
100	HgS	mp-1123	3.03	4.9	Theory	[27]	
101	CdF ₂	mp-241	2.96	4.3	Experiment	[17]	
102	LiCl ₂	mp-22905	2.74	3.5	Theory	[22]	
103	BaO	mp-1342	2.23	3.6	Theory	[27]	
104	AgI	mp-22925	2.19	2.02	Theory	[21]	
105	CsCdF ₃	mp-8399	1.87	1.73	Theory	[23]	
106	RbF	mp-11718	1.8	2.27	Experiment	[15]	
107	BaLiF ₃	mp-10250	1.77	2.21	Theory	[23]	
108	PbSe	mp-2201	1.47	1.55	Theory	[27]	
109	NaBr	mp-22916	1.43	3.25	Theory	[27]	
110	Ca ₅ Al ₂ Sb ₆	mp-8439	1.36	1.2	Experiment	[28]	
111	SrCl ₂	mp-23209	1.32	2.3	Experiment	[41]	
112	LiBr	mp-23259	1.18	1.83	Experiment	[15]	
113	PbTe	mp-19717	1.075	2.15	Theory	[27]	
114	NaI	mp-23268	1.03	2.1	Theory	[27]	
115	*SnSe	mp-691	0.78	0.8	Theory	[26]	
116	CsBr	mp-22906	0.69	0.94	Experiment	[42]	
117	CsHgF ₃	mp-561947	0.671	1.0	Theory	[23]	
118	TlBr	mp-568560	0.43	0.58	Experiment	[28]	

Continued on next page

Table S3: (continued)

Rank	Materials	mp-id	$\kappa_{MatterSim}^{BTE}$	κ_{ref}	κ_{ref}	Type	Source
119	Sn ₂ S ₃	mp-1509	0.064	0.06		Theory	[25]
120	RS-AgBr	mp-23231	0.24	0.25		Theory	[43]
121	WZ-AgI	mp-580941	1.30	1.42		Theory	[43]
122	ZB-AgI	mp-22925	1.90	2.22		Theory	[43]
123	RS-AgCl	mp-22922	0.23	0.29		Theory	[43]
124	WZ-AlAs	mp-8881	129.36	71.97		Theory	[43]
125	ZB-AlAs	mp-2172	163.28	87.41		Theory	[43]
126	RS-BaO	mp-1342	2.07	2.69		Theory	[43]
127	WZ-AlN	mp-661	225.37	229.73		Theory	[43]
128	ZB-AlN	mp-1700	228.76	222.00		Theory	[43]
129	RS-BaS	mp-1500	4.60	5.26		Theory	[43]
130	WZ-AlSb	mp-1018100	100.18	61.42		Theory	[43]
131	ZB-AlP	mp-1550	70.14	86.19		Theory	[43]
132	RS-BaSe	mp-1253	0.95	9.04		Theory	[43]
133	WZ-BAs	mp-984718	578.34	1395.87		Theory	[43]
134	ZB-AlSb	mp-2624	124.50	100.12		Theory	[43]
135	RS-BaTe	mp-1000	0.16	9.25		Theory	[43]
136	WZ-BP	mp-1008559	266.76	422.05		Theory	[43]
137	ZB-BAs	mp-10044	828.65	2004.66		Theory	[43]
138	RS-CaO	mp-2605	23.85	24.00		Theory	[43]
139	WZ-BeS	no-mp-4	90.82	130.84		Theory	[43]
140	ZB-BN	mp-1639	1075.16	1188.44		Theory	[43]
141	RS-CaS	mp-1672	25.73	29.73		Theory	[43]
142	WZ-BeSe	no-mp-3	102.45	314.99		Theory	[43]
143	ZB-BP	mp-1479	274.93	429.80		Theory	[43]
144	RS-CaSe	mp-1415	12.96	16.39		Theory	[43]
145	WZ-BeTe	mp-1183441	184.37	180.06		Theory	[43]
146	ZB-BeO	mp-1778	340.14	363.85		Theory	[43]
147	RS-CaTe	mp-1519	8.13	8.42		Theory	[43]
148	WZ-CuBr	no-mp-1	1.09	1.82		Theory	[43]

Continued on next page

Table S3: (continued)

Rank	Materials	mp-id	$\kappa_{MatterSim}^{BTE}$	κ_{ref}	κ_{ref}	Type	Source
149	ZB-BeS	mp-422	129.61	161.72	Theory	[43]	
150	RS-CdO	mp-1132	5.27	6.17	Theory	[43]	
151	WZ-CuCl	mp-1184046	0.44	0.83	Theory	[43]	
152	ZB-BeSe	mp-1541	175.88	383.34	Theory	[43]	
153	RS-CsF	mp-1784	0.85	1.34	Theory	[43]	
154	WZ-GaSb	mp-1018059	17.71	23.74	Theory	[43]	
155	ZB-BeTe	mp-252	187.05	282.23	Theory	[43]	
156	RS-KBr	mp-23251	0.89	2.45	Theory	[43]	
157	WZ-InN	mp-22205	72.72	110.78	Theory	[43]	
158	ZB-CdS	mp-2469	16.78	23.21	Theory	[43]	
159	RS-KCl	mp-23193	6.21	6.24	Theory	[43]	
160	WZ-InSb	mp-1007661	12.73	9.75	Theory	[43]	
161	ZB-CdSe	mp-2691	13.98	12.37	Theory	[43]	
162	RS-KF	mp-463	4.65	6.45	Theory	[43]	
163	WZ-MgTe	mp-1039	19.19	12.08	Theory	[43]	
164	ZB-CdTe	mp-406	7.93	6.95	Theory	[43]	
165	RS-KH	mp-24084	7.12	8.80	Theory	[43]	
166	WZ-ZnS	mp-561286	33.09	39.50	Theory	[43]	
167	ZB-CuBr	mp-22914	1.41	2.95	Theory	[43]	
168	RS-KI	mp-22898	0.08	1.25	Theory	[43]	
169	ZB-CuCl	mp-22905	0.53	1.44	Theory	[43]	
170	RS-LiBr	mp-23259	1.16	1.66	Theory	[43]	
171	ZB-CuH	no-mp-2	21.99	12.20	Theory	[43]	
172	RS-LiCl	mp-22905	3.19	3.50	Theory	[43]	
173	ZB-CuI	mp-22895	9.13	6.94	Theory	[43]	
174	RS-LiF	mp-1138	13.08	14.04	Theory	[43]	
175	ZB-GaAs	mp-2534	29.23	32.53	Theory	[43]	
176	RS-LiH	mp-23703	11.44	27.27	Theory	[43]	
177	ZB-GaN	mp-830	185.03	230.32	Theory	[43]	
178	RS-LiI	mp-22899	0.46	1.23	Theory	[43]	

Continued on next page

Table S3: (continued)

Rank	Materials	mp-id	$\kappa_{MatterSim}^{BTE}$	κ_{ref}	κ_{ref}	Type	Source
179	ZB-GaP	mp-2490	153.30	96.23	Theory	[43]	
180	RS-MgO	mp-1265	53.29	53.35	Theory	[43]	
181	ZB-GaSb	mp-1156	24.16	32.65	Theory	[43]	
182	RS-NaBr	mp-22916	1.36	2.43	Theory	[43]	
183	ZB-InAs	mp-20305	24.24	20.55	Theory	[43]	
184	RS-NaCl	mp-22862	6.23	7.13	Theory	[43]	
185	ZB-InN	mp-20411	76.08	99.05	Theory	[43]	
186	RS-NaF	mp-682	19.17	22.18	Theory	[43]	
187	ZB-InP	mp-20351	73.85	74.10	Theory	[43]	
188	RS-NaH	mp-23870	11.41	14.86	Theory	[43]	
189	ZB-InSb	mp-20012	14.45	12.66	Theory	[43]	
190	RS-NaI	mp-23268	0.98	1.27	Theory	[43]	
191	ZB-MgTe	mp-13033	28.39	16.39	Theory	[43]	
192	RS-PbS	mp-21276	1.72	1.21	Theory	[43]	
193	ZB-SiC	mp-8062	416.03	447.12	Theory	[43]	
194	RS-PbSe	mp-2201	1.08	0.73	Theory	[43]	
195	ZB-ZnO	mp-1986	68.36	63.99	Theory	[43]	
196	RS-PbTe	mp-19717	1.12	0.87	Theory	[43]	
197	ZB-ZnS	mp-10695	39.02	41.02	Theory	[43]	
198	RS-RbBr	mp-22867	0.33	3.12	Theory	[43]	
199	ZB-ZnSe	mp-1190	26.96	17.31	Theory	[43]	
200	RS-RbCl	mp-23295	0.51	1.85	Theory	[43]	
201	ZB-ZnTe	mp-2176	18.86	18.92	Theory	[43]	
202	RS-RbF	mp-11718	1.69	2.58	Theory	[43]	
203	RS-RbH	mp-24721	2.26	4.25	Theory	[43]	
204	RS-RbI	mp-22903	0.06	1.75	Theory	[43]	
205	RS-SrO	mp-2472	8.63	8.86	Theory	[43]	

S3 MatterK, database

S3.1 The database

A summary of all material entries with thermal conductivity predictions can be found in a separate file.

S3.2 Thermal conductivity phase diagram for RSS B-C-N chemical system and beyond

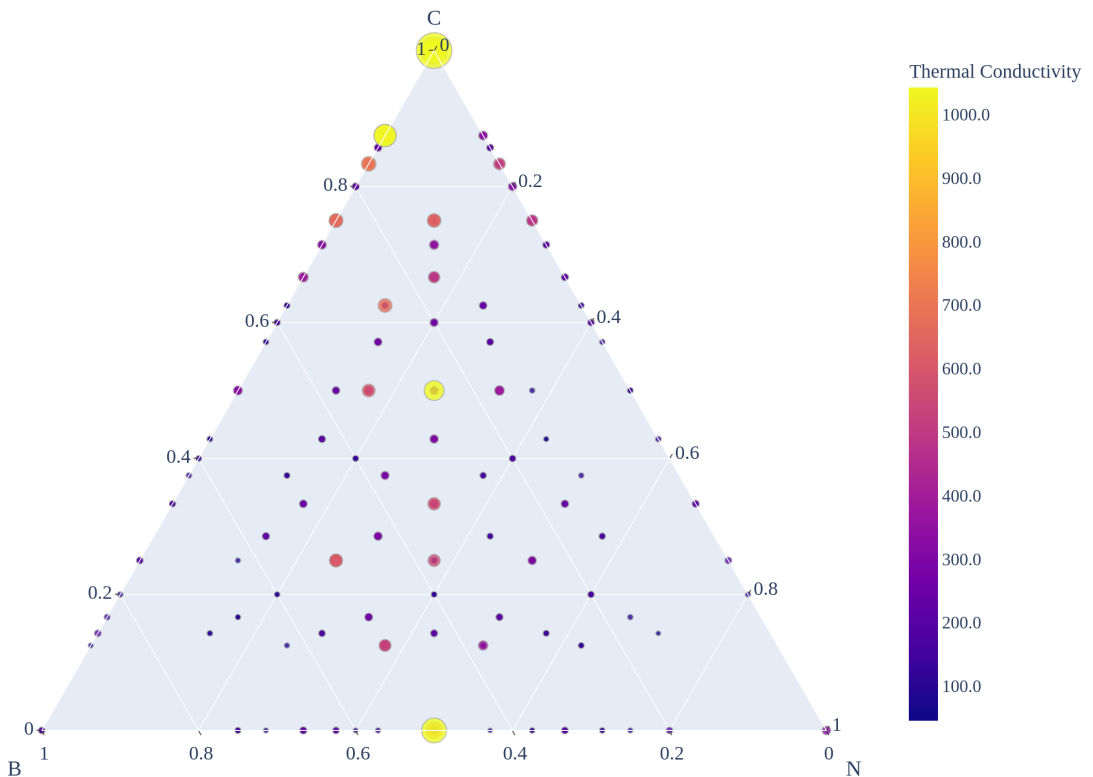


Fig. S4: Thermal conductivity phase diagram for B-C-N chemical system with structures generated through random structure search.

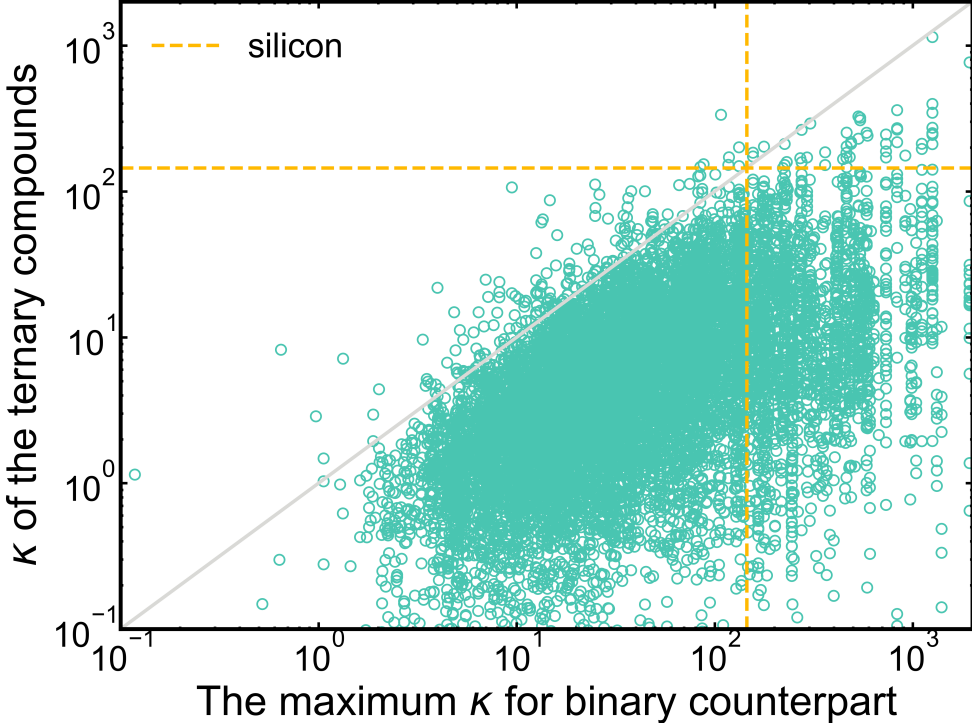


Fig. S5: Comparison of the κ values of ternary compounds with the maximum κ of their corresponding binary counterparts.

S3.3 Revisit the Slack's rule

Given this extensive data set, we revisit Slack's theory, which postulates that high thermal conductivity in nonmetals correlates with low atomic mass, strong bonding, simple crystal structure, and low anharmonicity [44]. Previous studies have demonstrated that low atomic mass alone is not a sufficient criterion, as materials with large mass ratios, such as BAs and TaN, can also exhibit outstanding thermal transport properties. Instead, the shear modulus—which serves as a proxy for bond strength—emerges as a more robust predictor of high thermal conductivity. The relationship between thermal conductivity and shear modulus (Fig. 3) supports this trend across a diverse range of materials, though with considerable spread. Notably, certain materials in the lower-right region of Fig. 3 exhibit strong elastic constants despite having low thermal conductivity, suggesting potential applications in thermal insulation and mechanical reinforcement.

High symmetry is often considered a key characteristic of materials with high thermal conductivity. However, our analysis of the correlation between thermal conductivity and crystal symmetry operations (Fig. S8) reveals no clear trend, suggesting that symmetry alone is not a decisive factor. For instance, BC₅ (mp-1386486), despite having only two symmetry operations, exhibits high thermal conductivity. In this layered material, the interlayer offsets disrupt its symmetry, yet it retains other key characteristics associated with high thermal transport. These findings indicate that, while

symmetry can influence thermal conductivity, additional factors-such as bonding strength, phonon dispersion, and scattering mechanisms-play a more dominant role.

S4 Thermal conductivity distributions

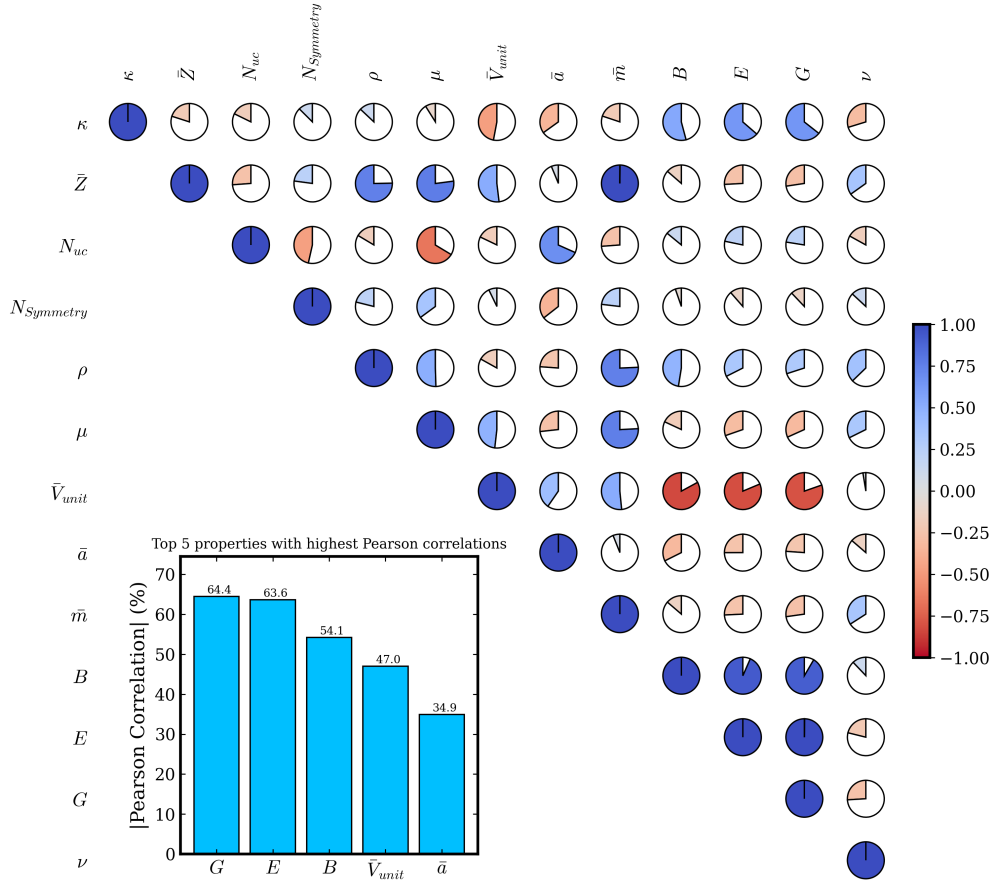


Fig. S6: Pearson correlation coefficients between a set of 12 material properties (Table S4) and κ computed through MatterSim-BTE for materials in Materials Project database[1]. Each pie chart represents the pairwise correlation coefficient between two properties. The color bar on the right ranges from -1.0 (strong negative correlation) to $+1.0$ (strong positive correlation). The bar chart at the lower right highlights the top five properties with the highest Pearson correlations (by absolute magnitude) across all pairs.

Table S4: List of material properties used in Pearson correlation analysis. Range indicates the minimum and maximum of the properties calculated with crystal structures from Material Project[1] using MatterSim.

Descriptions	Symbols	Units	Range
Shear modulus	G	GPa	[0.107, 517]
Young's modulus	E	GPa	[0.267, 1122.3]
Bulk modulus	B	GPa	[0.178, 463.5]
Poisson's ratio	ν	N/A	[0.003, 0.482]
Average lattice constants	\bar{a}	Å	[2.438, 20.716]
Average atomic number	\bar{Z}	N/A	[1.0, 94.0]
Average atomic masses	\bar{m}	a.m.u	[1.008, 244.1]
Normalized volume of the unit-cell	\bar{V}_{unit}	Å ³	[5.031, 583.2]
Number of cell symmetry operations	$N_{symmetry}$	N/A	[1, 48]
Number of atoms in the unit-cell	N_{uc}	N/A	[1, 15]
Global reduced masses [45]	μ	a.m.u	[0.084, 244.1]
Mass density	ρ	g cm ⁻³	[0.020, 22.547]

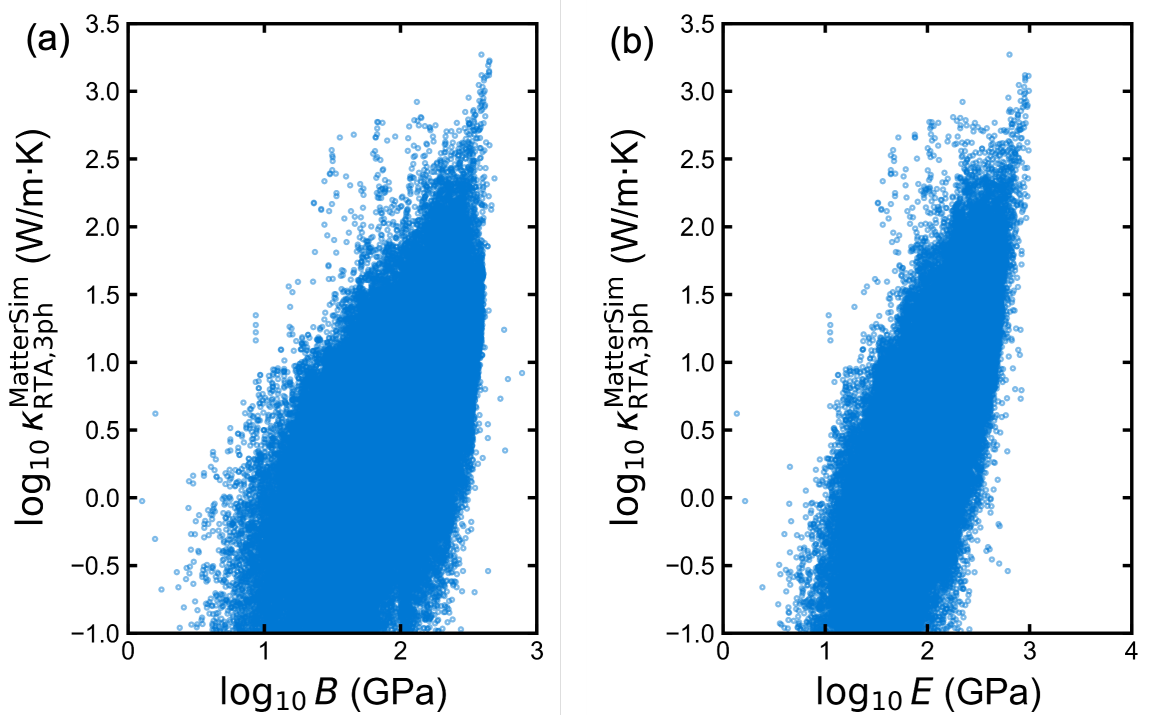


Fig. S7: The lattice thermal conductivity (under three-phonon scattering) distribution with respect to the Bulk modulus (B) and Young's modulus (E) for MatterK dataset.

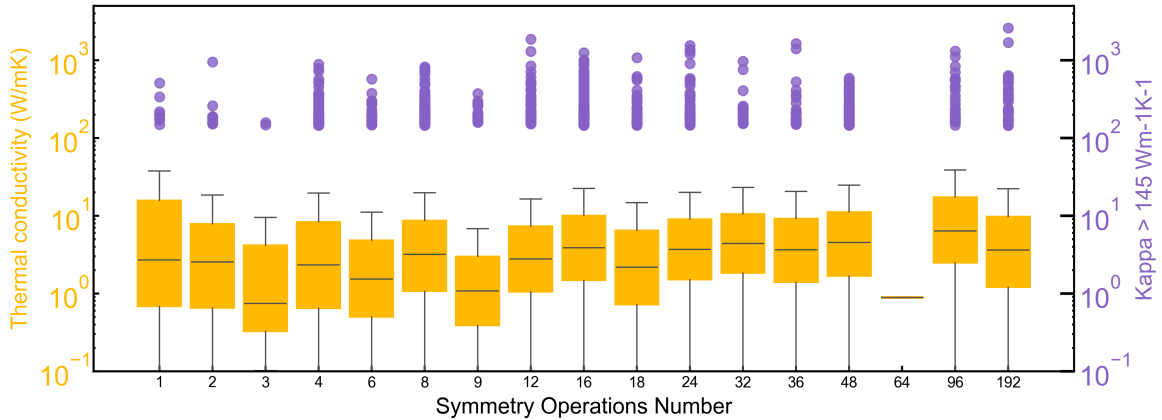


Fig. S8: The lattice thermal conductivity (under three-phonon scattering) distribution with respect to symmetry operation number determined through `get_symmetry_operations` function from pymatgen package[46].

S5 High thermal conductors

In this section, we listed all high thermal conductor candidates identified in this work. This includes: (1) Previously known high thermal conductors, as listed in [Table S5](#); (2) New high thermal conductors verified by DFT, listed in [Table 1](#) and [Table S6 - Table S7](#). Here, a "new" high thermal conductor is defined as a novel phase of a given chemical composition exhibiting a thermal conductivity exceeding that of silicon ($145 \text{ W m}^{-1} \text{ K}^{-1}$). (3) Unverified high thermal conductors predicted via large-scale near-first-principles calculations, performed using MatterSim-accelerated 3ph-BTE and provided in a separate supporting material.

Table S5: Summary of all known high thermal conductors. "band gap" (unit: eV) is the electronic band gap in the PBE level of theory. E_{hull} represents the energy above hull with the unit of eV/atom. κ shown in the table is in the unit of $\text{W m}^{-1} \text{K}^{-1}$. κ_{ref} stands for the reference κ values from the literature. The parentheses following the κ values indicate that the material is anisotropic, and the value inside the parentheses represents the κ values in other directions.

Systems	mp-id	space group	band gap	E_{hull}	$\kappa_{\text{RTA,3ph}}^{\text{MatterKappa}}$	κ_{ref}	κ_{ref} type	Source
Diamond	mp-66	Fd $\bar{3}$ m	4.1	0.14	1683	2000	Exp.	[44]
lonsdaleite(hex-C)	mp-47	P6 $_3$ /mmc	3.3	0.16	1580,1580,1494	1629,1629,1400	DFT-3ph	[47]
bct-C ₄	mp-1008395	I4/mmm	2.2	0.34	813,813,1293	1058,1058,1661	DFT-3ph	[47]
bct-C ₈	mp-570002	Im $\bar{3}$ m	3.0	0.77	703	715	DFT-3ph	[47]
m-carbon	mp-1080826	C2/m	3.5	0.30	992,670,640	494,849,622	DFT-3ph	[47]
Z-carbon	mp-1078845	Cmmm	3.3	0.27	1264,887,867	1262	DFT-3ph	[48]
c-BN	mp-1649	F $\bar{4}$ 3m	4.5	0.08	1111	768	Exp.	[49, 50]
h-BN	mp-2653	P6 $_3$ mc	5.2	0.09	853(838)	602(573)	DFT-3ph	[21]
BP	mp-1479	F $\bar{4}$ 3m	1.24	0.00	275	460	Exp.	[44, 51]
BP	mp-1008559	P6 $_3$ mc	1.1	0.01	267(228)	395(307)	DFT-3ph-iso	[21]
BA _s	mp-10044	F $\bar{4}$ 3m	1.2	0.08	849	1200	Exp.	[52–54]
BA _s	mp-984718	P6 $_3$ mc	1.1	0.09	646,646,550	1440,1440,1090	DFT-3ph-RTA	[21]
B ₂ AsP	mp-1008528	P4m2	1.1	0.07	268,268,185	372,372,308	DFT-3ph	[55]
c-SiC	mp-8062	F $\bar{4}$ 3m	1.4	0.00	465	490	Exp.	[56]
2H-SiC	mp-7140	P6 $_3$ mc	2.3	0.004	423(389)	497	DFT-3ph-iso	[57]
4H-SiC	mp-11714	P6 $_3$ mc	2.2	0.00	330(221)	415(345)	Exp.	[58]
6H-SiC	mp-7631	P6 $_3$ mc	2.0	0.00	296(256)	390(320)	Exp.	[58]
BeO	mp-1778	F $\bar{4}$ 3m	6.9	0.007	352	358	DFT-3ph-RTA	[21]
BeO	mp-2542	P6 $_3$ mc	7.4	0.00	278(288)	370	Exp.	[59]
AlN	mp-1700	F $\bar{4}$ 3m	3.3	0.02	233	212	DFT-3ph-RTA	[21]
AlN	mp-661	P6 $_3$ mc	4.05	0.00	221(235)	320	Exp.	[44]
GaN	mp-830	F $\bar{4}$ 3m	1.6	0.007	199	181	DFT-3ph	[21]
GaN	mp-804	P6 $_3$ mc	1.7	0.00	204.5(209.0)	200	Exp.	[58]
θ -TaN	mp-1459	P6m2	0.0	0.02	562(1057)	995(820)	DFT-4ph-epc-el	[60]
BC ₅	mp-1018649	P3m1	0.0	0.28	152(171)	165(169)	DFT-3ph	[61]
Si	mp-149	Fd $\bar{3}$ m	0.6	0.00	145	142	Exp.	[62]
WC	mp-1894	P6m2	0.0	0.00	1963.6(1733.2)	204(249)	DFT-3ph-epc-el	[63]
BiB	mp-1006880	F $\bar{4}$ 3m	0.1	0.82	587	347	DFT-3ph	[64]
GeC	mp-1002164	F $\bar{4}$ 3m	1.7	0.44	548	1517	DFT-3ph	[20]
2H-GeC	mp-1184550	P6 $_3$ mc	2.4	0.44	536,536,498	1350,1350,1050	DFT-3ph	[65]
BC ₂ N	mp-629458	Pmm2	1.7	0.54	677(449)	395	DFT-3ph	[66]
MoC	mp-2305	P6m2	0.0	0.00	573(494)	110	DFT-3ph-epc-el	[63]
BSb	mp-997618	F $\bar{4}$ 3m	0.8	0.27	469	465	DFT-3ph-iso	[3]
BC ₂ N	mp-30148	P222 ₁	2.1	0.55	491(439,424)	461	DFT-3ph	[66]
BeTe	mp-252	F $\bar{4}$ 3m	2.0	0.00	174	286	DFT-3ph-RTA	[21]
BeSe	mp-1541	F $\bar{4}$ 3m	2.7	0.00	168	633	DFT-3ph	[20]
Be	mp-87	P6 $_3$ /mmc	0.0	0.00	181(158)	200	Exp.	[67]

Table S6: Potential high- κ candidates verified by DFT at the level of BTE with three-phonon scattering. The structures are sourced from the Materials Project database (labeled with MP IDs) and an in-house random structure search database (labeled with RSS). The upper panel includes structures with a band gap, while the lower panel consists of structures without a band gap. The energy above the convex hull, E_{hull} , is reported in eV/atom, where higher values indicate greater thermodynamic instability for synthesis. Thermal conductivity values, κ , are given in $\text{W m}^{-1} \text{K}^{-1}$. $\kappa_{\text{RTA},3\text{ph}}^{\text{MatterSim}}$ represents values computed using MatterSim under the relaxation time approximation (RTA), considering only three-phonon scattering. $\kappa_{\text{LBTE}}^{\text{DFT}}$ denotes reference values obtained in this work via DFT using the full solution of the linearized phonon Boltzmann equation (LBTE). PBE functional is adopted in the DFT calculations unless otherwise specified. The Type column specifies the scattering processes considered in the DFT-BTE calculations: “3ph” (three-phonon scattering) contribution to thermal conductivity.

Systems	ID	Space Group	E_{hull}	$\kappa_{\text{RTA},3\text{ph}}^{\text{MatterSim}}$		Type
				xx yy zz	xx yy zz	
B ₆ O	mp-1346	R-3m	0.00	196 216 221	279 279 206	3ph
B ₆ P	mp-28395	R-3m	0.00	153 157 159	209 209 189	3ph
AlGaN ₂	mp-1228894	P3m1	0.01	159 159 126	181 181 144	3ph
SiGe	mp-1219182	F-43m	0.02	190 190 190	150 150 150	3ph
AlSiCN	mp-1227998	P3m1	0.04	228 228 145	317 317 275	3ph
WN ₂	mp-999549	P-6m2	0.09	219 219 241	436 436 517	3ph
WN ₂	mp-1077232	P6 ₃ /mmc	0.09	181 181 227	300 300 303	3ph
BP	RSS	R-3m	0.11	203 211 215	426 426 342	3ph
BP	RSS	P-6m2	0.14	226 226 189	388 388 244	3ph
BeSiN ₂	mp-1227309	P3m1	0.17	211 211 80	280 280 102	3ph
BN	mp-13151	P4 ₂ /mmn	0.18	648 348 348	451 451 1023	3ph
PtN ₂	mp-1095618	Pa-3	0.21	144 144 144	216 216 216	3ph
BN	mp-644751	Pnma	0.27	313 254 228	266 500 356	3ph
BN	mp-1077506	Imm2	0.30	141 251 249	184 304 324	3ph
CH [†]	mp-1079612	I2_13	0.32	185 185 185	536 536 536	3ph
CN ₂	mp-1018655	P-3m1	0.6	362 362 14	427 427 11	3ph
BC ₂ N	mp-1078541	C2/m	0.64	420 104 303	400 891 632	3ph
CN ₂	mp-1009818	I-4m2	0.73	223 228 231	399 399 216	3ph
BC ₂ N	mp-1008523	P-4m2	1.00	194 194 194	552 552 487	3ph
Be ₂ CoNi	mp-867271	Fm-3m	0.00	292 292 292	519 519 519	3ph
NbB	mp-2580	Cmcm	0.00	115 195 145	400 319 312	3ph
MnV ₂ Cr	mp-864953	Fm-3m	0.00	169 169 169	392 392 392	3ph
HfS	mp-1206743	P-6m2	0.00	82 82 302	247 247 352	3ph
VCr	RSS	Pm-3m	0.00	254 254 254	332 332 332	3ph
TaP	mp-1067587	I4 ₁ md	0.00	152 152 59	319 319 136	3ph
MnV	mp-316	Pm-3m	0.00	149 149 149	706 706 706	3ph
VB	RSS	Fm-3m	0.00	504 504 504	228 228 228	3ph
Al ₂ IrOs	mp-866284	Fm-3m	0.00	335 335 335	192 192 192	3ph
TaRe	RSS	Pm-3m	0.00	146 146 146	191 191 191	3ph
VN	mp-1018027	P-6m2	0.00	152 152 208	157 190 157	3ph
TaW	RSS	Pm-3m	0.00	146 146 146	190 190 190	3ph
B ₂ W	RSS	R-3m	0.00	179 168 164	118 118 158	3ph
MoWC ₂	mp-1221393	Pmm2	0.00	766 568 201	921 549 207	3ph
TmAl	RSS	Pm-3m	0.01	591 591 591	204 204 204	3ph
ReN	RSS	R3m	0.01	158 158 242	181 181 146	3ph
HoTmAl ₂	mp-1184827	Fm-3m	0.02	241 241 241	247 247 247	3ph

Continuation of Table S6

Systems	ID	Space Group	E_{hull}	$\kappa_{\text{RTA},3\text{ph}}^{\text{MatterSim}}$	$\kappa_{\text{LBTE}}^{\text{DFT}}$	Type
				xx yy zz	xx yy zz	
DyErAl ₂	mp-1183795	Fm-3m	0.02	230 230 230	207 207 207	3ph
CrC	mp-1018050	P-6m2	0.08	140 140 154	174 174 224	3ph
B ₂ CN	mp-1079333	Pmma	0.24	402 525 227	373 432 215	3ph
OsN ₂	mp-973935	P6/mmm	0.25	98 98 1322	97 97 931	3ph
BC ₅	mp-1077125	I-4m2	0.25	535 535 480	393 393 242	3ph
BC ₇	mp-1079046	Pmm2	0.25	1003 699 955	231 206 163	3ph
ReC	mp-1009735	P-6m2	0.27	369 369 328	225 225 362	3ph
BC ₇	mp-1095030	P-43m	0.28	1201 1201 1201	481 481 481	3ph
TiN	mp-998908	F-43m	0.30	312 312 312	199 199 199	3ph
C	mp-1008374	Cmmm	0.44	564 114 368	237 620 1157	3ph
BiB	mp-1183440	P6 ₃ mc	0.84	289 289 355	168 168 138	3ph

End of Table S6

* LDA functional is adopted in DFT calculations.

† K_4 phase of the carbon-hydrogen compound identified in Ref. 68.

Table S7: Potential high- κ candidates verified by DFT at the level of BTE with multiple scattering channels considered. The structures are sourced from the Materials Project database (labeled with MP IDs) and an in-house random structure search database (labeled with RSS). The energy above the convex hull, E_{hull} , is reported in eV/atom, where higher values indicate greater thermodynamic instability for synthesis. Thermal conductivity values, κ , are given in $\text{W m}^{-1} \text{K}^{-1}$. $\kappa_{\text{RTA},3\text{ph}}^{\text{MatterSim}}$ represents values computed using MatterSim under the relaxation time approximation (RTA), considering only three-phonon scattering. $\kappa_{\text{LBTE}}^{\text{DFT}}$ denotes reference values obtained in this work via DFT using the full solution of the linearized phonon Boltzmann equation (LBTE). PBE functional is adopted in the DFT calculations unless otherwise specified. The Type column specifies the scattering processes considered in the DFT-BTE calculations: “3ph” (three-phonon scattering), “4ph” (four-phonon scattering), “iso” (phonon-isotope scattering), “eph” (electron-phonon coupling), and “el” (electronic) contribution to thermal conductivity.

Systems	ID	Space Group	E_{hull}	$\kappa_{\text{RTA},3\text{ph}}^{\text{MatterSim}}$	$\kappa_{\text{LBTE}}^{\text{DFT}}$	Type
				xx yy zz	xx yy zz	
TaP*	mp-1187244	P-6m2	0.00	153 153 505	230 230 366	3ph+4ph+iso+eph+el
MnV	mp-316	Pm-3m	0.00	-	205 205 205	3ph+4ph+iso+eph+el
MnV*	mp-316	Pm-3m	0.00	-	243 243 243	3ph+4ph+iso+eph+el
ReB	RSS	P-6m2	0.00	231 231 199	90 90 158	3ph+iso+eph+el
MoWC ₂	mp-1221393	Pmm2	0.00	-	154 117 91	3ph+iso+eph+el
NbN	mp-2634	P-6m2	0.00	365 365 511	122 122 125	3ph+iso+eph+el
ZrN	mp-1352	Fm-3m	0.00	147 147 147	69 69 69	3ph+iso+eph+el
BeSe	mp-1541	F-43m	0.00	163 163 163	58 58 58	3ph+4ph+iso
CuBe	mp-2323	Pm-3m	0.00	404 404 404	44 44 44	3ph+4ph+iso
HfP	RSS	Fm-3m	0.02	635 635 635	42 42 42	3ph+4ph+iso
TaN*	mp-1459	P-6m2	0.03	540 540 1040	1023 1023 806	3ph+4ph+iso+eph+el
ZrP	mp-930	Fm-3m	0.04	605 605 605	31 31 31	3ph+iso+eph+el
WC	RSS	I4 ₁ md	0.14	833 833 525	294 294 198	3ph+iso+eph+el
TaN	mp-570604	P6 ₃ /mmc	0.24	159 159 186	48 48 54	3ph+iso+eph+el

Continuation of Table S7							
Systems	ID	Space Group	E_{hull}	$\kappa_{\text{RTA,3ph}}^{\text{MatterSim}}$	$\kappa_{\text{LBTE}}^{\text{DFT}}$	Type	
				xx yy zz	xx yy zz		
OsN ₂	mp-973935	P6/mmm	0.25	-	112 112 435	3ph+4ph+iso+eph+el	
BC ₇	mp-1095030	P-43m	0.28	-	74 74 74	3ph+iso+eph+el	
NbB	RSS	Fm-3m	0.29	2588 2588 2588	104 104 104	3ph+iso+eph+el	
BMo	RSS	Fm-3m	0.36	417 417 417	40 40 40	3ph+iso+eph+el	
ZrB	mp-451	Fm-3m	0.37	533 533 533	74 74 74	3ph+iso+eph+el	
BiB	mp-1006880	F-43m	0.82	585 585 585	168 168 168	3ph+4ph+iso	

End of [Table S7](#)

* LDA functional is adopted in DFT calculations.

† K_4 phase of the carbon-hydrogen compound identified in Ref. [68](#).

S6 Metals with novel thermal transport mechanism

S6.1 Detailed analysis for MnV, TiFe & ScCo

As discussed in the main text, the phonon dispersion relations reveal that all three acoustic phonon branches of MnV are degenerate at the high-symmetry R point. Additionally, the energy difference between the acoustic and optical phonon branches at the R point is small, leading to extended phonon lifetimes for frequencies beyond 8 THz. These prolonged phonon lifetimes result in a κ_{ph} as high as $661 \text{ W m}^{-1} \text{ K}^{-1}$, more than four times that of bulk Si, with isotopic scattering included in the calculations [\[38, 62, 69\]](#).

To further investigate the origin of this elevated κ_{ph} within the Boltzmann transport equation (BTE) framework considering three-phonon scattering, we analyzed the norm of the group velocity, phonon lifetimes, and modal conductivity ($\kappa_{\text{per mode}}$) along high-symmetry directions in the Brillouin zone ([Fig. S12](#)). The collective analysis of these three quantities indicates that, in addition to the dominant contributions near the Γ point, phonon modes around the R point significantly enhance κ_{ph} . A similar trend has previously been reported in *bcc* elementary metals such as W, Mo, and Cr [\[70\]](#).

Further calculations account for four-phonon and electron-phonon scattering processes. Electron-phonon coupling reduces κ_{ph} to $153 \text{ W m}^{-1} \text{ K}^{-1}$, while four-phonon scattering further lowers it to $119 \text{ W m}^{-1} \text{ K}^{-1}$. A detailed analysis of MnV is presented in the main text.

In addition to MnV, similar analyses have been conducted for the binary intermetallic materials TiFe and ScCo, which also crystallize in the *bcc* structure. Notably, TiFe emerges as a promising candidate, with $\kappa_{\text{ph}} \simeq 200$ when only three-phonon (3ph) scattering is considered. Like MnV, TiFe

exhibits phonon degeneracy at the R point in the Brillouin zone, though the energy difference between its optical and acoustic phonons is larger. Consequently, the scattering rate is enhanced for phonons near R point, and the phonon lifetime is suppressed due to the increased phase space available for energy- and momentum-conserving three-phonon processes.

This trend is further confirmed by the analysis of ScCo, which distinguishes itself from MnV and TiFe by exhibiting an even larger energy difference between its optical and acoustic phonons near R point, leading to a further reduction in κ_{ph} .

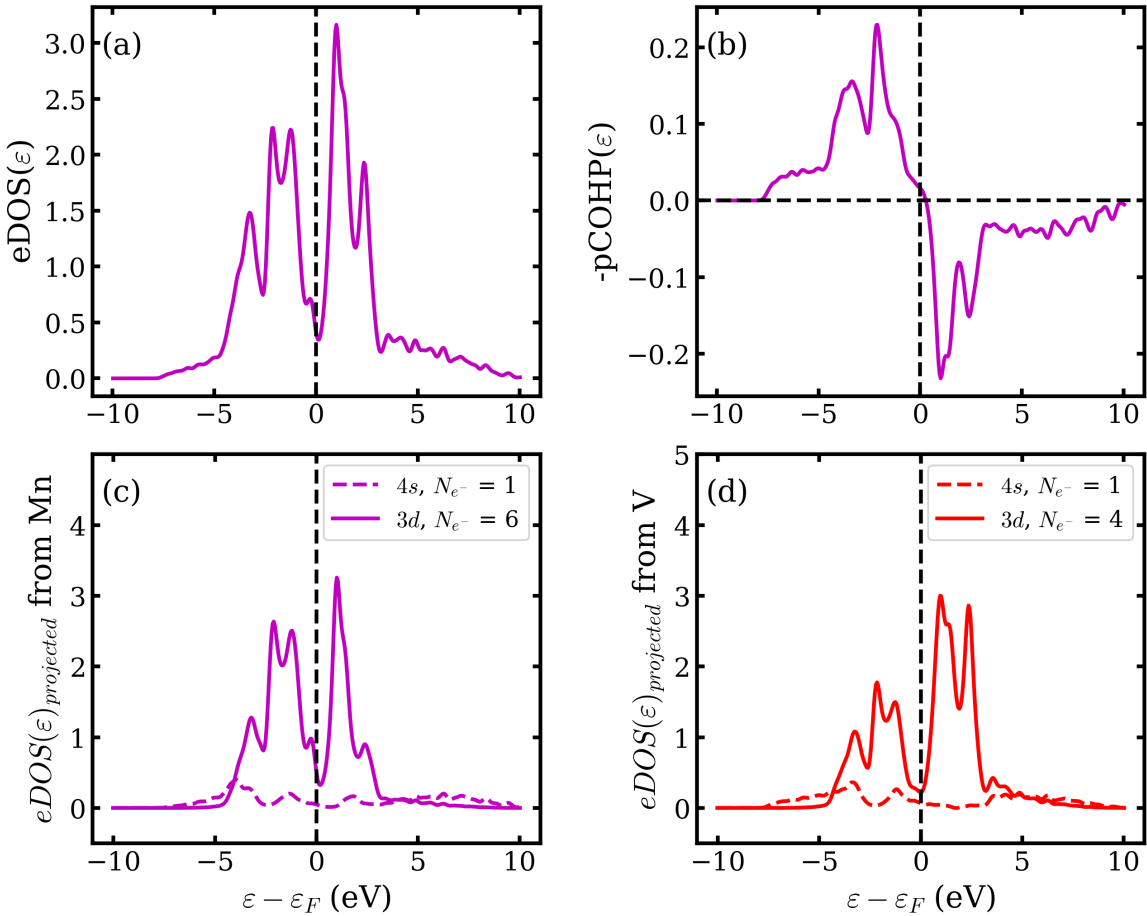


Fig. S9: Total electronic density of state (eDOS) (a) and projected crystal orbital Hamilton population (pCOHP) (b) for MnV in the Pm-3m phase. (c) and (d) represent the projection of electronic DOS ($e\text{DOS}(\varepsilon)_{\text{projected}}$) for Mn and V atoms. N_{e^-} symbolizes number of electrons contributing to bonding in 4s and 3d orbitals, obtained by integrating the $e\text{DOS}(\varepsilon)_{\text{projected}}$ up to Fermi energy (ε_F).

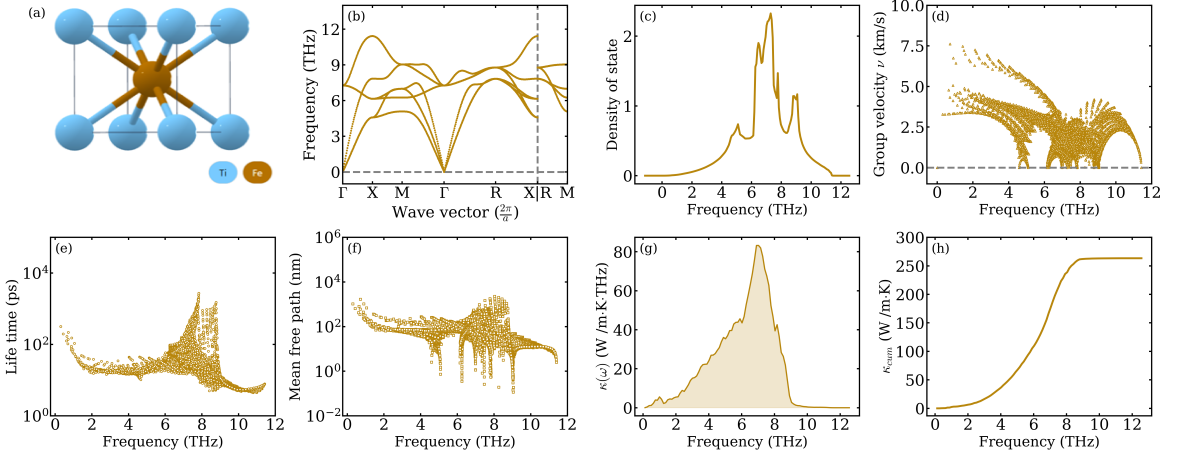


Fig. S10: Unit-cell structure of TiFe in Pm-3m phase with its phononic and thermal transport properties. When accounting for three-phonon scattering, κ_{cum} reaches to $263 \text{ W m}^{-1} \text{ K}^{-1}$.

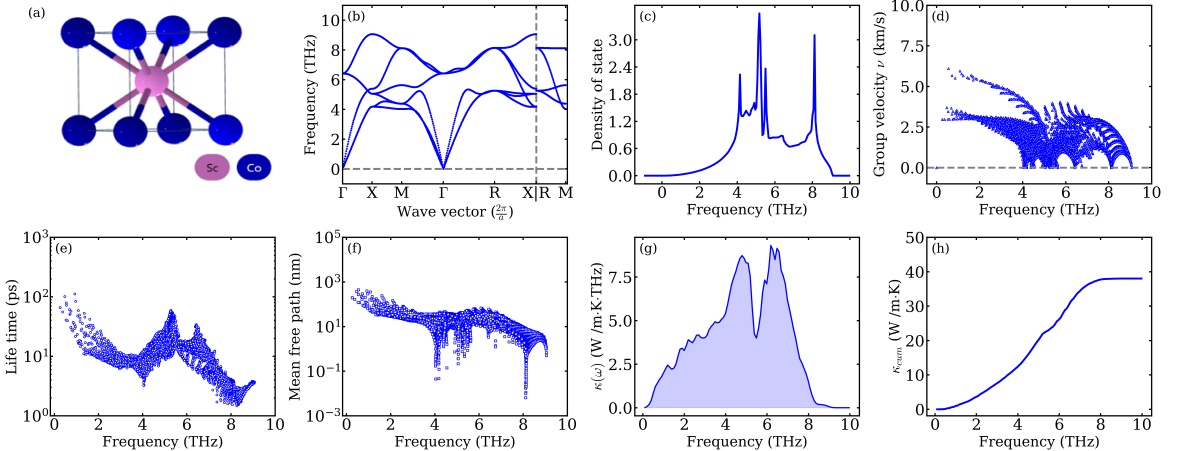


Fig. S11: Unit-cell structure of ScCo in Pm-3m phase with phononic and its thermal transport properties. Upon including three-phonon scattering, κ_{cum} reaches to $38.1 \text{ W m}^{-1} \text{ K}^{-1}$

Table S8: Summary of space group symmetry, lattice constants as well as κ_{ph} for metallic compounds along each axis. The unit of κ_{ph} is in $\text{W m}^{-1} \text{ K}^{-1}$.

materials	space group	a	b	c	κ_{xx}	κ_{yy}	κ_{zz}	κ_{type}
MnV	Pm-3m	2.875 Å	2.875 Å	2.875 Å	119	119	119	3ph + 4ph + eph + iso
TiFe	Pm-3m	2.956 Å	2.956 Å	2.956 Å	263	263	263	3ph
ScCo	Pm-3m	3.120 Å	3.120 Å	3.120 Å	38.1	38.1	38.1	3ph
OsN ₂	P6/mmm	2.836 Å	2.836 Å	4.956 Å	24.0	24.0	212	3ph + 4ph + eph
TaP	P $\bar{6}$ m2	3.266 Å	3.266 Å	3.302 Å	201	201	316	3ph + 4ph + eph

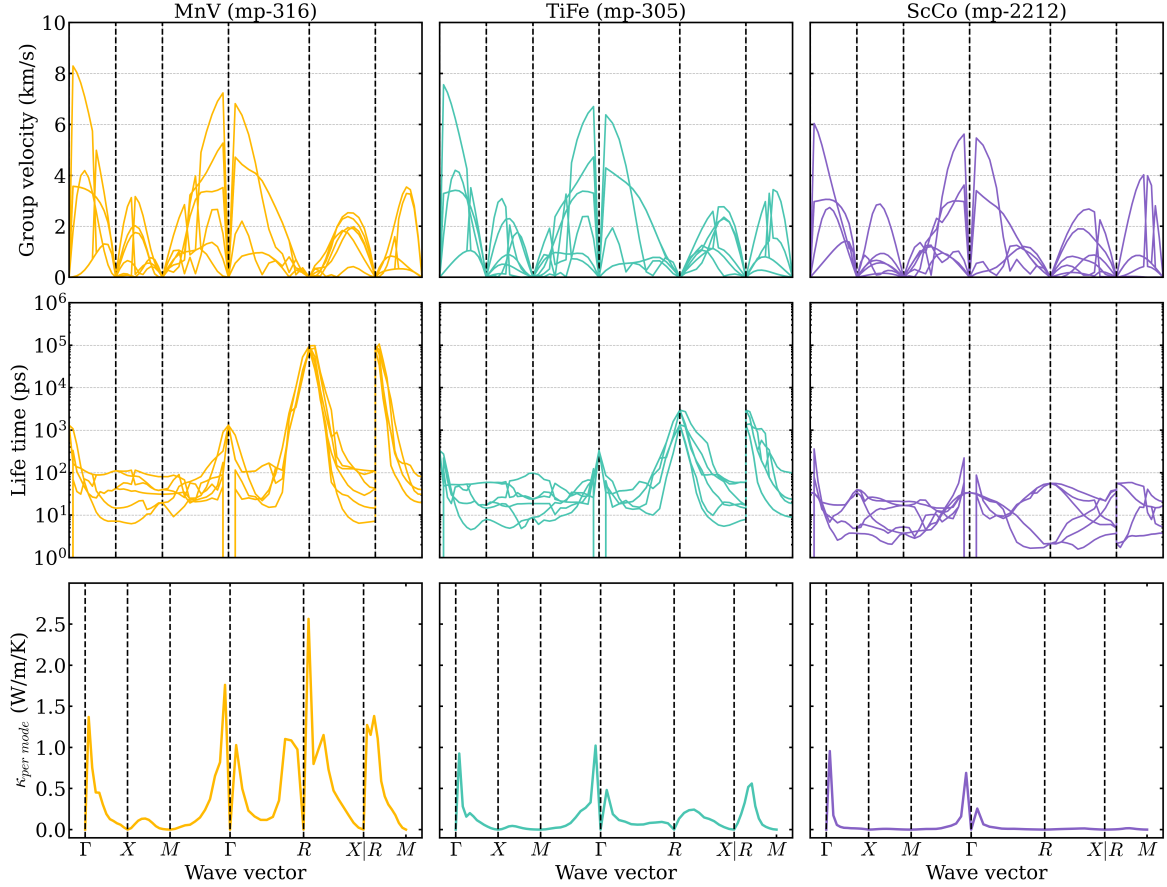


Fig. S12: Norm of phonon group velocities, life time and per mode thermal conductivity ($\kappa_{\text{per mode}}$) for MnV, TiFe and ScCo. Lattice dynamic calculations are performed with DFT-based interatomic force constants using a $4 \times 4 \times 4$ super-cell and a q -grid of $32 \times 32 \times 32$. Note that the phonon life time is computed with tetrahedral method and used in tandem with RTA method to obtain $\kappa_{\text{per mode}}$, as implemented in phono3py[71].

References

- [1] Jain, A., Ong, S.P., Hautier, G., Chen, W., Richards, W.D., Dacek, S., Cholia, S., Gunter, D., Skinner, D., Ceder, G., et al.: Commentary: The materials project: A materials genome approach to accelerating materials innovation. *APL materials* **1**(1) (2013)
- [2] Ward, A., Broido, D., Stewart, D.A., Deinzer, G.: Ab initio theory of the lattice thermal conductivity in diamond. *Physical Review B* **80**(12), 125203 (2009)
- [3] Lindsay, L., Broido, D., Reinecke, T.: First-principles determination of ultrahigh thermal conductivity of boron arsenide: a competitor for diamond? *Physical review letters* **111**(2), 025901 (2013)
- [4] McGaughey, A.J., Jain, A., Kim, H.-Y., Fu, B.: Phonon properties and thermal conductivity from first principles, lattice dynamics, and the boltzmann transport equation. *Journal of Applied Physics* **125**(1) (2019)
- [5] Slack, G., Newman, R.: Thermal conductivity of mno and nio. *Physical Review Letters* **1**(10), 359 (1958)
- [6] LaBotz, R.J., Mason, D.R.: The thermal conductivities of mg2si and mg2ge. *Journal of The Electrochemical Society* **110**(2), 121 (1963)
- [7] Martin, J.: Thermal conductivity of mg2si, mg2ge and mg2sn. *Journal of physics and chemistry of solids* **33**(5), 1139–1148 (1972)
- [8] Martin, J., Shanks, H.: Thermal conductivity of magnesium plumbide. *Journal of Applied Physics* **45**(6), 2428–2431 (1974)
- [9] Takahashi, T., Kikuchi, T.: Porosity dependence on thermal diffusivity and thermal conductivity of lithium oxide li2o from 200 to 900° c. *Journal of Nuclear Materials* **91**(1), 93–102 (1980)
- [10] Slack, G.A., Andersson, P.: Pressure and temperature effects on the thermal conductivity of cucl. *Physical Review B* **26**(4), 1873 (1982)
- [11] Morelli, D., Caillat, T., Fleurial, J.-P., Borshchevsky, A., Vandersande, J., Chen, B., Uher, C.: Low-temperature transport properties of p-type cosb 3. *Physical Review B* **51**(15), 9622 (1995)
- [12] Hohl, H., Ramirez, A.P., Goldmann, C., Ernst, G., Wölfling, B., Bucher, E.: Efficient dopants for zrnisn-based thermoelectric materials. *Journal of Physics: Condensed Matter* **11**(7), 1697 (1999)

- [13] Young, D., Khalifah, P., Cava, R.J., Ramirez, A.: Thermoelectric properties of pure and doped femsb ($m = v$, nb). *Journal of Applied Physics* **87**(1), 317–321 (2000)
- [14] Kawaharada, Y., Kuroski, K., Muta, H., Uno, M., Yamanaka, S.: High temperature thermo-electric properties of cotisb half-heusler compounds. *Journal of alloys and compounds* **384**(1-2), 308–311 (2004)
- [15] Morelli, D.T., Slack, G.A.: High lattice thermal conductivity solids. In: *High Thermal Conductivity Materials*, pp. 37–68. Springer, ??? (2006)
- [16] Mann, M., Thompson, D., Serivalsatit, K., Tritt, T.M., Ballato, J., Kolis, J.: Hydrothermal growth and thermal property characterization of tho₂ single crystals. *Crystal growth & design* **10**(5), 2146–2151 (2010)
- [17] Popov, P., Fedorov, P., Osiko, V.: Thermal conductivity of single crystals with a fluorite structure: cadmium fluoride. *Physics of the Solid State* **52**, 504–508 (2010)
- [18] Toberer, E.S., Zevalkink, A., Snyder, G.J.: Phonon engineering through crystal chemistry. *Journal of Materials Chemistry* **21**(40), 15843–15852 (2011)
- [19] Xiao, W., Tan, D., Zhou, W., Liu, J., Xu, J.: Cubic perovskite polymorph of strontium metasilicate at high pressures. *American Mineralogist* **98**(11-12), 2096–2104 (2013)
- [20] Lindsay, L., Broido, D., Reinecke, T.: Phonon-isotope scattering and thermal conductivity in materials with a large isotope effect: A first-principles study. *Physical Review B—Condensed Matter and Materials Physics* **88**(14), 144306 (2013)
- [21] Togo, A., Chaput, L., Tanaka, I.: Distributions of phonon lifetimes in brillouin zones. *Physical review B* **91**(9), 094306 (2015)
- [22] Seko, A., Togo, A., Hayashi, H., Tsuda, K., Chaput, L., Tanaka, I.: Prediction of low-thermal-conductivity compounds with first-principles anharmonic lattice-dynamics calculations and bayesian optimization. *Physical review letters* **115**(20), 205901 (2015)
- [23] Roekeghem, A., Carrete, J., Oses, C., Curtarolo, S., Mingo, N.: High-throughput computation of thermal conductivity of high-temperature solid phases: the case of oxide and fluoride perovskites. *Physical Review X* **6**(4), 041061 (2016)
- [24] Zhao, Y., Dai, Z., Zhang, C., Lian, C., Zeng, S., Li, G., Meng, S., Ni, J.: High thermopower and potential thermoelectric properties of crystalline lih and nah. *Physical Review B* **95**(1), 014307

(2017)

- [25] Skelton, J.M., Burton, L.A., Jackson, A.J., Oba, F., Parker, S.C., Walsh, A.: Lattice dynamics of the tin sulphides sns 2, sns and sn 2 s 3: vibrational spectra and thermal transport. *Physical Chemistry Chemical Physics* **19**(19), 12452–12465 (2017)
- [26] Xie, Y., Zhou, Y., Gong, X.-G.: The intrinsic low lattice thermal conductivity in the rock salt snse. *Computational Materials Science* **148**, 54–59 (2018)
- [27] Xia, Y., Hegde, V.I., Pal, K., Hua, X., Gaines, D., Patel, S., He, J., Aykol, M., Wolverton, C.: High-throughput study of lattice thermal conductivity in binary rocksalt and zinc blende compounds including higher-order anharmonicity. *Physical Review X* **10**(4), 041029 (2020)
- [28] Zhu, T., He, R., Gong, S., Xie, T., Gorai, P., Nielsch, K., Grossman, J.C.: Charting lattice thermal conductivity for inorganic crystals and discovering rare earth chalcogenides for thermoelectrics. *Energy & Environmental Science* **14**(6), 3559–3566 (2021)
- [29] Rakesh Roshan, S., Yedukondalu, N., Muthaiah, R., Lavanya, K., Anees, P., Kumar, R.R., Rao, T.V., Ehm, L., Parise, J.B.: Anomalous lattice thermal conductivity in rocksalt iia–via compounds. *ACS Applied Energy Materials* **5**(1), 882–896 (2021)
- [30] Tranås, R., Løvvik, O.M., Tomic, O., Berland, K.: Lattice thermal conductivity of half-heuslers with density functional theory and machine learning: Enhancing predictivity by active sampling with principal component analysis. *Computational Materials Science* **202**, 110938 (2022)
- [31] Cao, W., Shi, J., Xiong, R., Miao, L., Wang, Z., Liu, Z.: Anomalous thermal transport in mgse with diamond phase under pressure. *Physical Review B* **107**(23), 235201 (2023)
- [32] Miller, S.A., Gorai, P., Ortiz, B.R., Goyal, A., Gao, D., Barnett, S.A., Mason, T.O., Snyder, G.J., Lv, Q., Stevanović, V., *et al.*: Capturing anharmonicity in a lattice thermal conductivity model for high-throughput predictions. *Chemistry of Materials* **29**(6), 2494–2501 (2017)
- [33] Zhang, Y., Ling, C.: A strategy to apply machine learning to small datasets in materials science. *Npj Computational Materials* **4**(1), 25 (2018)
- [34] Chen, L., Tran, H., Batra, R., Kim, C., Ramprasad, R.: Machine learning models for the lattice thermal conductivity prediction of inorganic materials. *Computational Materials Science* **170**, 109155 (2019)
- [35] De Jong, M., Chen, W., Angsten, T., Jain, A., Notestine, R., Gamst, A., Sluiter, M.,
27

- Krishna Ande, C., Van Der Zwaag, S., Plata, J.J., *et al.*: Charting the complete elastic properties of inorganic crystalline compounds. *Scientific data* **2**(1), 1–13 (2015)
- [36] Wen, M., Horton, M.K., Munro, J.M., Huck, P., Persson, K.A.: An equivariant graph neural network for the elasticity tensors of all seven crystal systems. *Digital Discovery* **3**(5), 869–882 (2024)
- [37] Ju, S., Yoshida, R., Liu, C., Wu, S., Hongo, K., Tadano, T., Shiomi, J.: Exploring diamond-like lattice thermal conductivity crystals via feature-based transfer learning. *Physical Review Materials* **5**(5), 053801 (2021)
- [38] Qian, X., Peng, S., Li, X., Wei, Y., Yang, R.: Thermal conductivity modeling using machine learning potentials: application to crystalline and amorphous silicon. *Materials Today Physics* **10**, 100140 (2019)
- [39] Jha, A.R.: Rare Earth Materials: Properties and Applications. CRC Press, ??? (2014)
- [40] Campi, D., Paulatto, L., Fugallo, G., Mauri, F., Bernasconi, M.: First-principles calculation of lattice thermal conductivity in crystalline phase change materials: GeTe, Sb_2Te_3 , and $\text{Ge}_2\text{Sb}_2\text{Te}_5$. *Physical Review B* **95**(2), 024311 (2017)
- [41] Moore, J., Weaver, F., Graves, R., McElroy, D.: The thermal conductivities of SrCl_2 and SrF_2 from 85 to 400 K. *Thermal Conductivity* **18**, 115–124 (1985)
- [42] Gerlich, D., Andersson, P.: Temperature and pressure effects on the thermal conductivity and heat capacity of CsCl , CsBr and CsI . *Journal of Physics C: Solid State Physics* **15**(25), 5211 (1982)
- [43] Póta, B., Ahlawat, P., Csányi, G., Simoncelli, M.: Thermal conductivity predictions with foundation atomistic models. arXiv preprint arXiv:2408.00755 (2024)
- [44] Slack, G.A.: Nonmetallic crystals with high thermal conductivity. *Journal of Physics and Chemistry of Solids* **34**(2), 321–335 (1973)
- [45] Purcell, T.A., Scheffler, M., Ghiringhelli, L.M., Carbogno, C.: Accelerating materials-space exploration for thermal insulators by mapping materials properties via artificial intelligence. *npj Computational Materials* **9**(1), 112 (2023)
- [46] Ong, S.P., Richards, W.D., Jain, A., Hautier, G., Kocher, M., Cholia, S., Gunter, D., Chevrier, V.L., Persson, K.A., Ceder, G.: Python materials genomics (pymatgen): A robust, open-source python library for materials analysis. *Computational Materials Science* **68**, 314–319 (2013)

- [47] Xiao, Y., Wang, J., Zhao, Y., Meng, S., Dai, Z.: High thermal conductivity of carbon allotropes and its relationship with mechanical properties: A first-principles study. *International Journal of Thermal Sciences* **176**, 107481 (2022)
- [48] Wang, F.Q., Hu, M., Wang, Q.: Ultrahigh thermal conductivity of carbon allotropes with correlations with the scaled pugh ratio. *Journal of Materials Chemistry A* **7**(11), 6259–6266 (2019)
- [49] Novikov, N.: Thermal conductivity of single crystals of cubic boron nitride. *Dopov. Akad. Nauk Ukr. RSR, Ser. A*, 72 (1983)
- [50] Chen, K., Song, B., Ravichandran, N.K., Zheng, Q., Chen, X., Lee, H., Sun, H., Li, S., Udalammata Gamage, G.A.G., Tian, F., *et al.*: Ultrahigh thermal conductivity in isotope-enriched cubic boron nitride. *Science* **367**(6477), 555–559 (2020)
- [51] Kang, J.S., Wu, H., Hu, Y.: Thermal properties and phonon spectral characterization of synthetic boron phosphide for high thermal conductivity applications. *Nano letters* **17**(12), 7507–7514 (2017)
- [52] Kang, J.S., Li, M., Wu, H., Nguyen, H., Hu, Y.: Experimental observation of high thermal conductivity in boron arsenide. *Science* **361**(6402), 575–578 (2018)
- [53] Li, S., Zheng, Q., Lv, Y., Liu, X., Wang, X., Huang, P.Y., Cahill, D.G., Lv, B.: High thermal conductivity in cubic boron arsenide crystals. *Science* **361**(6402), 579–581 (2018)
- [54] Tian, F., Song, B., Chen, X., Ravichandran, N.K., Lv, Y., Chen, K., Sullivan, S., Kim, J., Zhou, Y., Liu, T.-H., *et al.*: Unusual high thermal conductivity in boron arsenide bulk crystals. *Science* **361**(6402), 582–585 (2018)
- [55] Liu, Z., Jiang, M., Luo, T.: Leveraging low-fidelity data to improve machine learning of sparse high-fidelity thermal conductivity data via transfer learning. *Materials Today Physics* **28**, 100868 (2022)
- [56] Slack, G.A.: Thermal conductivity of pure and impure silicon, silicon carbide, and diamond. *Journal of Applied physics* **35**(12), 3460–3466 (1964)
- [57] Protik, N.H., Katre, A., Lindsay, L., Carrete, J., Mingo, N., Broido, D.: Phonon thermal transport in 2h, 4h and 6h silicon carbide from first principles. *Materials Today Physics* **1**, 31–38 (2017)

- [58] Zheng, Q., Li, C., Rai, A., Leach, J.H., Broido, D.A., Cahill, D.G.: Thermal conductivity of gan, gan 71, and sic from 150 k to 850 k. *Physical Review Materials* **3**(1), 014601 (2019)
- [59] Slack, G.A., Austerman, S.: Thermal conductivity of beo single crystals. *Journal of Applied Physics* **42**(12), 4713–4717 (1971)
- [60] Kundu, A., Yang, X., Ma, J., Feng, T., Carrete, J., Ruan, X., Madsen, G.K., Li, W.: Ultrahigh thermal conductivity of θ -phase tantalum nitride. *Physical Review Letters* **126**(11), 115901 (2021)
- [61] Muthaiah, R., Garg, J., Arafat, S.: Ultrahard bc5—an efficient nanoscale heat conductor through dominant contribution of optical phonons. *Computational Materials Science* **206**, 111276 (2022)
- [62] Shanks, H., Maycock, P., Sidles, P., Danielson, G.: Thermal conductivity of silicon from 300 to 1400 k. *Physical Review* **130**(5), 1743 (1963)
- [63] Kundu, A., Ma, J., Carrete, J., Madsen, G., Li, W.: Anomalously large lattice thermal conductivity in metallic tungsten carbide and its origin in the electronic structure. *Materials Today Physics* **13**, 100214 (2020)
- [64] Li, C., Broido, D.: Phonon thermal transport in transition-metal and rare-earth nitride semiconductors from first principles. *Physical Review B* **95**(20), 205203 (2017)
- [65] Muthaiah, R., Garg, J.: First principles investigation of high thermal conductivity in hexagonal germanium carbide (2h-gec). *Carbon Trends* **5**, 100113 (2021)
- [66] Abdullah, N.R., Azeez, Y.H., Tang, C.-S., Gudmundsson, V.: High thermal conductivity of orthorhombic bc2n semiconductor: Dft study of electronic, phonon, aimd, and optical properties. *Diamond and Related Materials* **148**, 111455 (2024)
- [67] Chen, Y., Pang, G., Meng, F., Li, W.: Origin of the high lattice thermal conductivity of beryllium among the elemental metals. *Physical Review B* **109**(22), 220302 (2024)
- [68] Lian, C.-S., Wang, X.-Q., Wang, J.-T.: Hydrogenated k4 carbon: A new stable cubic gauche structure of carbon hydride. *The Journal of Chemical Physics* **138**(2) (2013)
- [69] Barbalinardo, G., Chen, Z., Lundgren, N.W., Donadio, D.: Efficient anharmonic lattice dynamics calculations of thermal transport in crystalline and disordered solids. *Journal of Applied Physics* **128**(13) (2020)

- [70] Chen, Y., Ma, J., Wen, S., Li, W.: Body-centered-cubic structure and weak anharmonic phonon scattering in tungsten. *npj Computational Materials* **5**(1), 98 (2019)
- [71] Togo, A.: First-principles phonon calculations with phonopy and phono3py. *Journal of the Physical Society of Japan* **92**(1), 012001 (2023)